LETTER

doi:10.1038/nature11930

Critical role of Trib1 in differentiation of tissue-resident M2-like macrophages

Takashi Satoh[1,2], Hiroyasu Kidoya[3], Hisamichi Naito[3], Masahiro Yamamoto[4,5], Naoki Takemura[1,2], Katsuhiro Nakagawa[1,2], Yoshichika Yoshioka[6], Eiichi Morii[7], Nobuyuki Takakura[3], Osamu Takeuchi[1,2,8] & Shizuo Akira[1,2]

Macrophages consist of at least two subgroups, M1 and M2 (refs 1–3). Whereas M1 macrophages are proinflammatory and have a central role in host defence against bacterial and viral infections[4,5], M2 macrophages are associated with responses to anti-inflammatory reactions, helminth infection, tissue remodelling, fibrosis and tumour progression[6]. Trib1 is an adaptor protein involved in protein degradation by interacting with COP1 ubiquitin ligase[7]. Genome-wide association studies in humans have implicated TRIB1 in lipid metabolism[8–10]. Here we show that Trib1 is critical for the differentiation of F4/80$^+$MR$^+$ tissue-resident macrophages—that share characteristics with M2 macrophages (which we term M2-like macrophages)—and eosinophils but not for the differentiation of M1 myeloid cells. Trib1 deficiency results in a severe reduction of M2-like macrophages in various organs, including bone marrow, spleen, lung and adipose tissues. Aberrant expression of C/EBPα in Trib1-deficient bone marrow cells is responsible for the defects in macrophage differentiation. Unexpectedly, mice lacking Trib1 in haematopoietic cells show diminished adipose tissue mass accompanied by evidence of increased lipolysis, even when fed a normal diet. Supplementation of M2-like macrophages rescues the pathophysiology, indicating that a lack of these macrophages is the cause of lipolysis. In response to a high-fat diet, mice lacking Trib1 in haematopoietic cells develop hypertriglyceridaemia and insulin resistance, together with increased proinflammatory cytokine gene induction. Collectively, these results demonstrate that Trib1 is critical for adipose tissue maintenance and suppression of metabolic disorders by controlling the differentiation of tissue-resident M2-like macrophages.

Members of the tribble family are pseudokinase proteins that are conserved among species and implicated in various human diseases, such as leukaemia and metabolic disorders. Tribble proteins interact with an E3 ubiquitin ligase, COP1, for protein degradation. In thioglycollate-elicited macrophages, Trib1 is important for interleukin (IL)-12p40 production to lipopolysaccharide[11]. In addition, Trib1 and Trib2 have been implicated in acute myeloid leukaemia[12,13]. Trib3 can inhibit insulin signalling[14], although *Trib3*$^{-/-}$ mice do not show defects in insulin signalling or glucose homeostasis[15]. However, the roles of tribble proteins in haematopoietic cell development have not been clarified.

First, we examined the populations of tissue-resident macrophages in mice lacking tribble family genes in the spleen. Although the proportions of B cells, T cells, dendritic cells and Ly6C^{high}Mac1$^+$ inflammatory monocytes were not altered between wild-type and *Trib1*$^{-/-}$ splenocytes, F4/80$^+$Mac1$^+$ macrophages, which also expressed Mrc1 (also called MR), *Arg1* and *Fizz1* (also called *Retnla*), were markedly reduced and Siglec-F$^+$CCR3$^+$ eosinophils were absent in *Trib1*$^{-/-}$ spleens (Fig. 1a and Supplementary Figs 1 and 2). In contrast, the neutrophil population was increased in *Trib1*$^{-/-}$ spleens (Fig. 1a and Supplementary Fig. 3). Splenic F4/80$^+$ red pulp macrophages phagocytose aged red blood cells and accumulate iron[16,17]. Immunohistochemical staining of spleen sections confirmed the absence of red pulp macrophages in *Trib1*$^{-/-}$ spleen (Fig. 1b). Furthermore, Perl's Prussian blue staining of the spleen sections revealed that iron did not accumulate in *Trib1*$^{-/-}$ mice (Fig. 1c and Supplementary Fig. 4). In contrast, splenic metallophilic and marginal zone macrophages were normal in *Trib1*$^{-/-}$ mice (Supplementary Fig. 5). In addition to the spleen, tissue-resident macrophages in other tissues were severely decreased in *Trib1*$^{-/-}$ mice; however, peritoneal resident macrophages were comparable between wild-type and *Trib1*$^{-/-}$ mice (Supplementary Fig. 6). Newly generated *Trib2*$^{-/-}$ and *Trib3*$^{-/-}$ mice did not show any defects in myeloid and lymphoid cells in the spleen (Supplementary Figs 7 and 8). Because MR, Arg1 and Fizz1 expression is a hallmark characteristic of M2 macrophages, we termed this population M2-like macrophages. Thus, these findings indicate that Trib1 is critical for the differentiation of tissue-resident M2-like macrophages and eosinophils in the peripheral organs.

Differentiation of haematopoietic cells, including macrophages, occurs in the bone marrow, followed by their migration to peripheral tissues via the bloodstream. Consistent with the defects observed in peripheral organs, numbers of F4/80$^+$Mac1$^+$ cells and Siglec-F$^+$CCR3$^+$ eosinophils were severely decreased in the blood and bone marrow cells from *Trib1*$^{-/-}$ mice whereas numbers of Gr-1^{high} neutrophils were slightly increased (Fig. 1d, e). However, inflammatory monocytes were comparable between wild-type and *Trib1*$^{-/-}$ bone marrow cells (Supplementary Fig. 9). The adoptive transfer of *Trib1*$^{-/-}$ bone marrow cells to wild-type mice failed to increase F4/80$^+$ macrophage numbers in the bone marrow and spleen (data not shown). Furthermore, competitive transfer of CD45.1$^+$ wild-type and CD45.2$^+$ *Trib1*$^{-/-}$ bone marrow cells (1:1 ratio) to sublethal-irradiated wild-type mice led to severely impaired development of CD45.2$^+$ macrophages and eosinophils, and increased the population of neutrophils (Supplementary Fig. 10). These findings demonstrate that the defects observed in *Trib1*$^{-/-}$ mice are intrinsic to haematopoietic cells, and that Trib1 is critical for regulating the proper differentiation of myeloid cells in the bone marrow. To delineate the developmental competency of *Trib1*$^{-/-}$ bone marrow cells, we performed colony-forming assays. Whereas granulocyte/neutrophil colonies were increased, macrophage colonies were severely decreased and eosinophil colonies were not generated in *Trib1*$^{-/-}$ bone marrow cells compared with wild-type cells (Fig. 2a). We found that macrophage colonies could be morphologically classified into two subgroups, namely aggregated/small and diffused/large macrophages (Fig. 2b). Although most wild-type macrophage colonies were aggregated and small, the macrophage colonies obtained from *Trib1*$^{-/-}$ bone marrow cells were diffused and large (Fig. 2b). These results indicated that Trib1 is essential for the proper

[1]Laboratory of Host Defense, WPI Immunology Frontier Research Center (WPI IFReC), Osaka University, 3-1 Yamada-oka, Suita, Osaka 565-0871, Japan. [2]Department of Host Defense, Research Institute for Microbial Diseases (RIMD), Osaka University, 3-1 Yamada-oka, Suita, Osaka 565-0871, Japan. [3]Department of Signal Transduction, Research Institute for Microbial Diseases (RIMD), Osaka University, 3-1 Yamada-oka, Suita, Osaka 565-0871, Japan. [4]Laboratory of immunoparasitology, WPI Immunology Frontier Research Center (WPI IFReC), Osaka University, 3-1 Yamada-oka, Suita, Osaka 565-0871, Japan. [5]Department of Immunoparasitology, Research Institute for Microbial Diseases (RIMD), Osaka University, 3-1 Yamada-oka, Suita, Osaka 565-0871, Japan. [6]Laboratory of Biofunctional Imaging, WPI Immunology Frontier Research Center (WPI IFReC), Osaka University, 3-1 Yamada-oka, Suita, Osaka 565-0871, Japan. [7]Department of Pathology, Graduate School of Medicine, Osaka University, 2-2 Yamada-oka, Suita, Osaka 565-0871, Japan. [8]Laboratory of Infection and Prevention, Institute for Virus Research, Kyoto University, 53 Shogoin Kawara-cho, Sakyo-ku, Kyoto 606-8507, Japan.

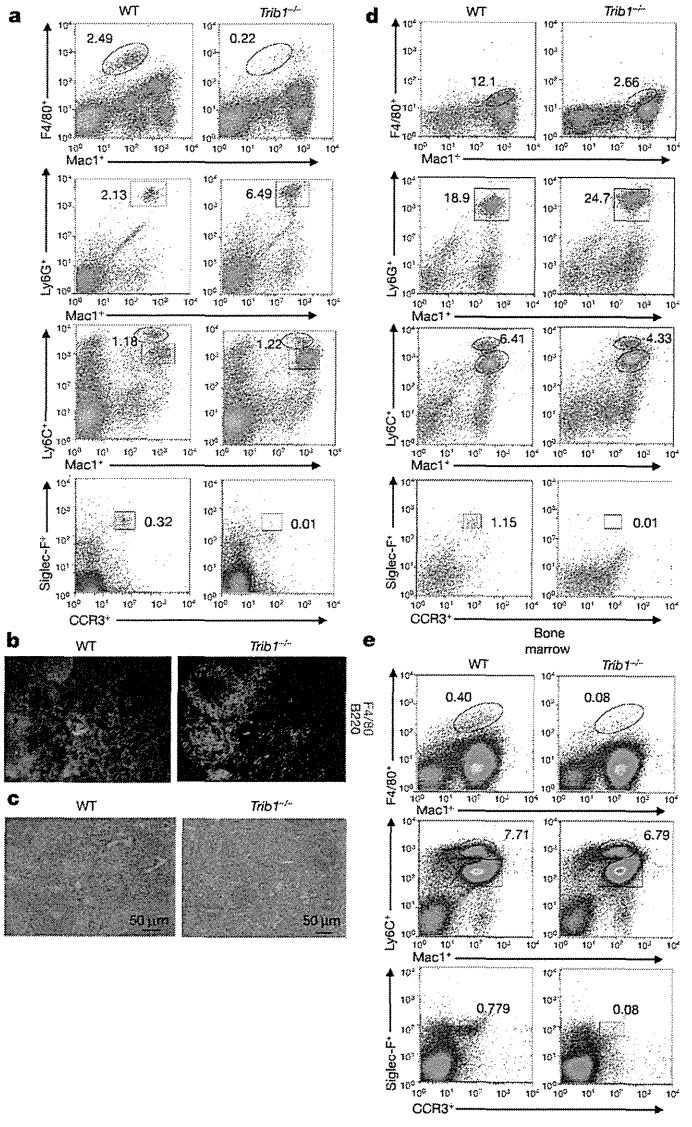

Figure 1 | Lack of tissue-resident M2-like macrophages and eosinophils in *Trib1*-deficient mice. **a**, Flow cytometric analyses of splenocytes. The expression levels of F4/80$^+$ and Mac1$^+$ tissue-resident M2-like macrophages in splenocytes are shown (top). The proportions of inflammatory monocytes and neutrophils (middle) and eosinophils (bottom) in splenocytes are also shown. Similar results were obtained in eight independent experiments. **b**, Wild-type (WT) and *Trib1*$^{-/-}$ spleen sections were stained for F4/80 (red) and B220 (green). **c**, Images of Perl's Prussian blue staining for ferric iron in the spleens of wild-type and *Trib1*$^{-/-}$ mice. Scale bars, 50 μm. **d**, Flow cytometric analysis of cell populations in the blood. The percentages of F4/80$^+$ and Mac1$^+$ cells in the blood are shown. **e**, Flow cytometric analysis of bone marrow. The percentages of F4/80$^+$ and Mac1$^+$ tissue-resident M2-like macrophages in the bone marrow are shown (top). The proportions of inflammatory monocytes and neutrophils (middle) and eosinophils (bottom) in the bone marrow are also shown. Similar results were obtained in three independent experiments (**b**–**e**).

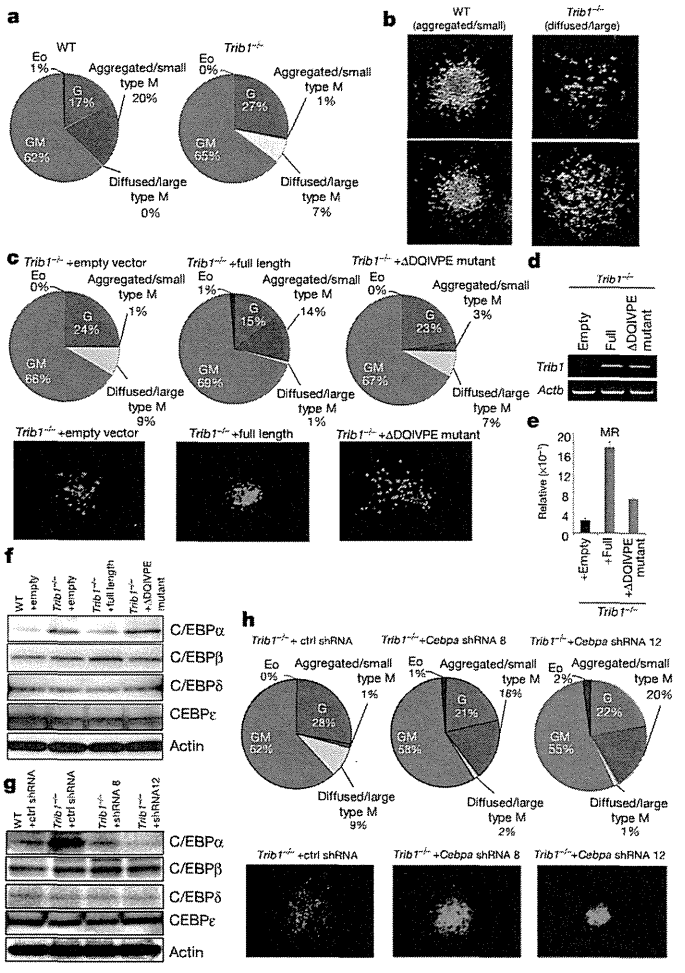

Figure 2 | Trib1 controls macrophage, eosinophil and neutrophil differentiation via the ubiquitin-binding domain. **a**, **b**, Bone marrow cells were subjected to colony-forming assays. Each colony was counted depending on the morphology (**a**), and images of the cell types of macrophage colonies are shown (**b**). Eo, eosinophil colonies; G, granulocyte/neutrophil colonies; GM, granulocyte/macrophage colonies; M, macrophage colonies. **c**–**e**, Role of the COP1-binding site in macrophage differentiation. Bone marrow cells lacking *Trib1* were infected with retroviruses expressing empty vector, full-length Trib1 (mTrib1) or Trib1(ΔDQIVPE) mutant. Colony-forming assays were performed in retrovirus-infected (GFP$^+$) cells. Images of the retrovirus-infected (GFP$^+$) cell types of macrophage colonies are shown in **c**. **d**, Semi-quantitative PCR analyses were performed to measure the expression of *Trib1* in empty vector, full-length Trib1 (full length) or mutant Trib1(ΔDQIVPE) in macrophage colonies. **e**, Quantitative PCR analyses were performed for MR expression in macrophage colonies expressing empty vector, Trib1 (full length) or mutant Trib1(ΔDQIVPE). Error bars indicate s.d. of duplicates. Similar results were obtained in three independent experiments (**a**–**e**). **f**, Immunoblot analyses of various C/EBP family molecules. Lineage-negative fractions from wild-type, *Trib1*$^{-/-}$ cells, *Trib1*$^{-/-}$ cells expressing full-length and *Trib1*$^{-/-}$ cells expressing mutant Trib1(ΔDQIVPE) were analysed by western blotting. **g**, **h**, Role of C/EBPα in macrophage differentiation. Bone marrow cells lacking *Trib1* were infected with retroviruses expressing empty vector, *Cebpa* shRNA 8 or *Cebpa* shRNA 12. Immunoblot analyses of various C/EBP family molecules. Lineage-negative fractions from wild-type, *Trib1*$^{-/-}$ cells and *Trib1*$^{-/-}$ cells expressing *Cebpa* shRNA 8 or *Cebpa* shRNA 12 were analysed by western blotting (**g**). Colony-forming assays were performed in infected (GFP$^+$) cells, and images of the retrovirus-infected (GFP$^+$) cell types of macrophage colonies are shown (**h**). Similar results were obtained in two independent experiments (**f**–**h**).

differentiation of bone marrow myeloid cells. Proportions of CMP and CLP as well as GMP were comparable between wild-type and *Trib1*$^{-/-}$ mice (see Supplementary Fig. 11 for definitions). Furthermore, the expression pattern of transcriptional factors, which are involved in myeloid cell differentiation, in GMP and MDP was also comparable between wild-type and *Trib1*$^{-/-}$ mice (Supplementary Fig. 12), suggesting that Trib1 controls myeloid cell differentiation downstream of GMP.

Retroviral expression of full-length Trib1 in *Trib1*$^{-/-}$ bone marrow cells resulted in a marked increase in aggregated and small macrophage colonies and eosinophil colonies, but decreased granulocyte/neutrophil colonies (Fig. 2c, d and Supplementary Fig. 13). In contrast, expression of Trib1 lacking the COP1-binding site (Trib1(ΔDQIVPE) mutant) in *Trib1*$^{-/-}$ bone marrow cells failed to restore the differentiation defects. Moreover, expression of full-length Trib1, but not of

Trib1(ΔDQIVPE) mutant, restored expression of M2 macrophage marker genes such as *MR* (Fig. 2e). Next, we investigated the expression of potential target proteins of the Trib1–COP1 axis in *Trib1*$^{-/-}$ bone marrow cells. Among the transcription factors, C/EBP family members are important for determining the balance between granulopoiesis and monopoiesis[18]. We found that expression of C/EBPα, but not other transcriptional factors involved in myeloid cell differentiation, was increased in lineage-negative bone marrow cells and macrophage colonies lacking Trib1 (Fig. 2f and Supplementary Fig. 14). The expression of full-length Trib1 in *Trib1*$^{-/-}$ bone marrow cells suppressed the level of C/EBPα expression (Fig. 2f). To address whether increased expression of C/EBPα is involved in aberrant myeloid cell differentiation under Trib1 deficiency, we genetically inhibited *Cebpa* in *Trib1*$^{-/-}$ bone marrow cells using short hairpin RNAs (shRNAs) (Supplementary Fig. 15). The decreased C/EBPα protein expression in *Trib1*$^{-/-}$ bone marrow cells was similar to levels of

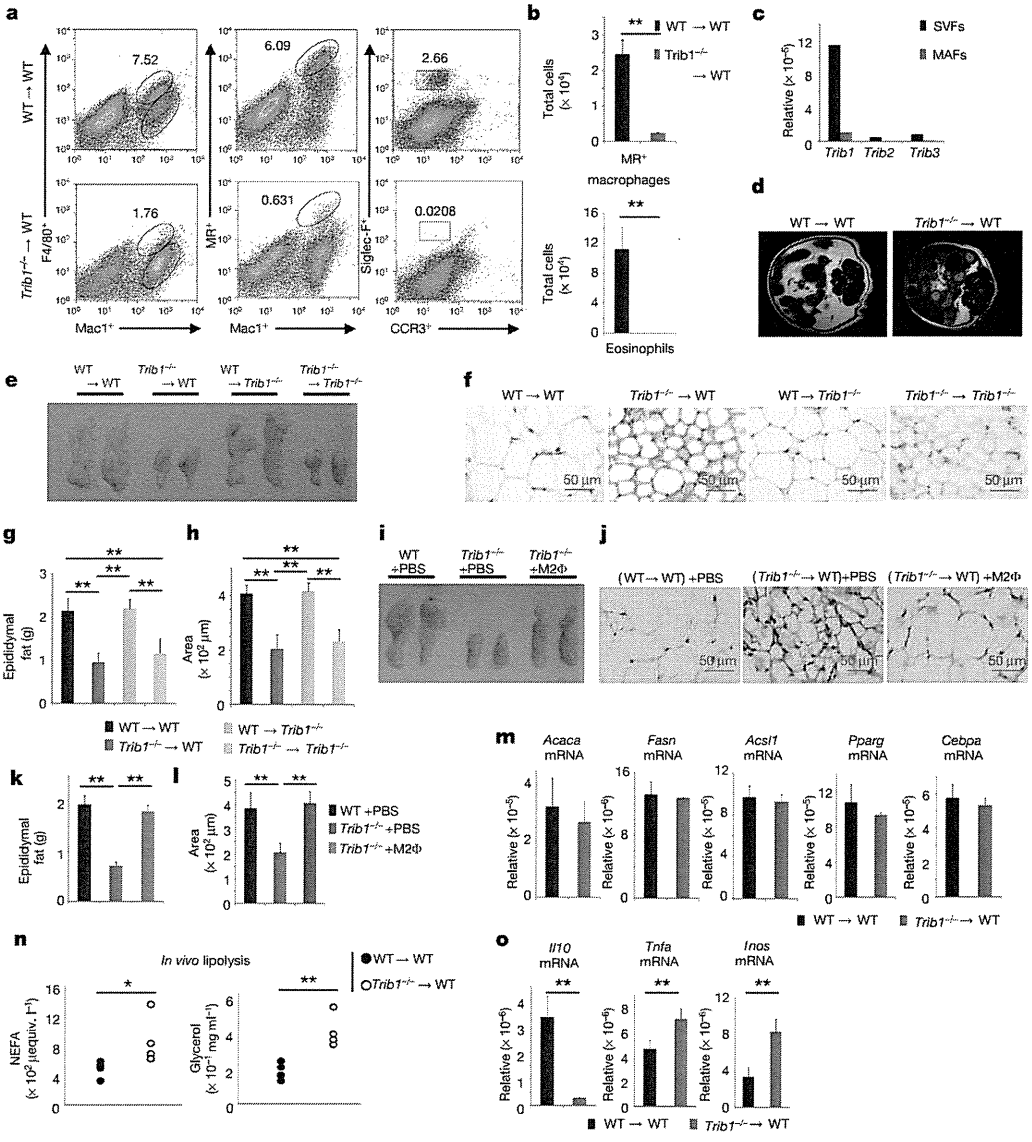

Figure 3 | Impact of Trib1 deficiency on lipodystrophy. a, b, Flow cytometric analyses of haematopoietic cells in adipose tissue. The expression levels of F4/80$^+$ and Mac1$^+$ or MR$^+$ and Mac1$^+$ tissue-resident M2 macrophages in adipose tissue (left and centre) and Siglec-F$^+$ and CCR3$^+$ eosinophils (right) are shown. The total numbers of MR$^+$ macrophages and eosinophils in adipose tissues from wild-type and *Trib1*$^{-/-}$ chimaeric mice fed a normal diet are shown (**b**). Error bars indicate s.d. of duplicates. Similar results were obtained in three independent experiments. **c,** Expression levels of *Trib1*, *Trib2* and *Trib3* in SVFs and MAFs, assessed by quantitative PCR. Similar results were obtained in two independent experiments. **d,** The epididymal adipose tissues from wild-type and *Trib1*$^{-/-}$ chimaeric mice fed a normal diet were analysed by magnetic resonance imaging (MRI). **e,** Images of the epididymal adipose tissues from each indicated chimaeric mice fed a normal diet are shown. **f,** Haematoxylin and eosin-stained images of paraffin-embedded epididymal adipose tissue sections from each indicated chimaeric mice fed a normal diet. Scale bars, 50 μm. **g, h,** The total epididymal fat weight was measured (**g**) and each area of adipocytes was measured (**h**) in each indicated chimaeric mouse. Error bars indicate s.d. of duplicates. **i,** Images of the epididymal adipose tissues from each indicated chimaeric mice fed a normal diet are shown. **j,** Haematoxylin-and-eosin-stained images of paraffin-embedded epididymal adipose tissue sections from each indicated chimaeric mice fed a normal diet. Scale bars, 50 μm. **k, l,** The total epididymal fat weight (**k**) and each area of adipocytes were measured (**l**) in each indicated chimaeric mouse. Error bars indicate s.d. of duplicates. **m,** Total RNA was prepared from wild-type and *Trib1*$^{-/-}$ chimaeric mice fed a normal diet. The expression levels of mRNAs encoding the indicated proteins were determined by quantitative PCR. Error bars indicate s.d. of duplicates. Similar results were obtained in three independent experiments (**e**–**m**). **n,** Lipolysis assays in wild-type and *Trib1*$^{-/-}$ mice fed a normal diet. The serum glycerol and NEFA levels were measured *in vivo*. Similar results were obtained in two independent experiments. **o,** Total RNA was prepared from wild-type and *Trib1*$^{-/-}$ chimaeric mice fed a normal diet. The expression levels of mRNAs encoding the indicated proteins were determined by quantitative PCR. Error bars indicate s.d. of duplicates. Similar results were obtained in three independent experiments. Statistical significance in **b, g, h, k, l, n, o** was determined using the Student's *t*-test. $^*P < 0.05$; $^{**}P < 0.01$.

wild-type cells (Fig. 2g). Repression of *Cebpa* resulted in an increase in the aggregated and small macrophage colonies and eosinophil colonies, but a decrease in granulocyte/neutrophil colonies (Fig. 2h). Taken together, these data demonstrate that Trib1 regulates myeloid cell differentiation by altering the expression of C/EBPα in a COP1-dependent manner.

Recent genome-wide association studies revealed that genetic variants in the loci corresponding to *TRIB1* are associated with increased plasma lipoprotein concentrations, a high risk of ischaemic heart disease and myocardial infarction in humans[8–10]. These studies prompted us to investigate the role of Trib1 in the adipose tissue and liver of mice. Because we did not observe histological changes in the liver in the absence of Trib1 in mice fed normal chow (Supplementary Fig. 16), we next examined the adipose tissues. Consistent with observations in other organs, $MR^+F4/80^+$ adipose-tissue-resident M2-like macrophages were severely decreased in the stromal vascular fraction (SVF) derived from *Trib1*$^{-/-}$ epididymal adipose tissues compared with wild-type mice (Supplementary Fig. 17). Mice lacking Trib1 in haematopoietic cells also showed a reduced number of M2-like macrophages and lacked eosinophils in epididymal adipose tissues (Fig. 3a, b), and *Trib1* mRNA was rarely expressed in the normal mature adipocyte fraction (MAF) (Fig. 3c), indicating that the defect is intrinsic to haematopoietic cells. In contrast, $CD11c^+Mac1^+$ M1 macrophages were hardly present in wild-type and *Trib1*$^{-/-}$ adipose tissues from mice fed a normal chow diet (Supplementary Fig. 17). Unexpectedly, MRI analyses revealed that Trib1 deficiency in haematopoietic cells severely reduced the abdominal adipose tissues (Fig. 3d). The epididymal adipose tissues and size of each epididymal adipocyte were significantly smaller in mice lacking Trib1 in all tissues as well as in haematopoietic cells only, than in littermate wild-type mice fed a normal diet (Fig. 3e–h). Thus, the mice showed a lipodystrophic phenotype. In contrast, *Trib1*$^{-/-}$ mice harbouring wild-type haematopoietic cells did not develop lipodystrophy (Fig. 3e, f). These findings demonstrate that Trib1 deficiency in haematopoietic cells is responsible for development of this pathophysiology. To investigate whether loss of M2-like macrophages is responsible for the development of lipodystrophy, we supplemented *Trib1*$^{-/-}$ mice with these macrophages (Supplementary Fig. 18). After 3 weeks, the epididymal adipose tissues and the size of each adipocyte from *Trib1*$^{-/-}$ mice reconstituted with these macrophages were significantly larger than in PBS-treated *Trib1*$^{-/-}$ mice (Fig. 3i–l). Collectively, these data indicate that lack of M2-like macrophages, caused by Trib1 deficiency, is important for the development of the lipodystrophic phenotype.

Next, we examined the mechanisms of the lipodystrophy caused by Trib1 deficiency in haematopoietic cells. Adipose tissues are maintained by balance between lipogenesis and lipolysis. The mRNA levels of genes involved in adipocyte differentiation and lipogenesis were comparable between wild-type and *Trib1*$^{-/-}$ bone marrow chimaeric mice (Fig. 3m and Supplementary Fig. 19; see Methods). In contrast, the serum levels of non-esterified fatty acids (NEFAs) and glycerol were significantly elevated in *Trib1*$^{-/-}$ bone marrow chimaeric mice (Fig. 3n), indicative of enhanced lipolysis caused by Trib1 deficiency. Cytokines produced by macrophages contribute to adipose tissue inflammation and lipolysis. Expression of IL-10 was severely reduced in epididymal adipose tissues lacking Trib1 in haematopoietic cells. In contrast, *Tnf* and *Inos* mRNA expression were elevated in adipose tissues from *Trib1*$^{-/-}$ bone marrow chimaeric mice (Fig. 3o). Because several reports indicated that IL-10 has a central role in repressing lipolysis in adipocytes in addition to having anti-inflammatory effects[19–21], it is possible that M2-like macrophages are important for maintaining adipose tissues, at least in part, through the production of IL-10. However, the contribution of additional molecules produced by the macrophages may also be critical for amelioration of lipodystrophy.

Lipodystrophy is often associated with metabolic abnormalities. Although significant differences in levels of the parameters such as serum glucose, cholesterol, triglyceride and insulin were not detected between wild-type and *Trib1*$^{-/-}$ bone marrow chimaeric mice fed a normal diet, the feeding of mice with a high-fat diet (HFD) led to much higher elevations of these parameters in the serum of *Trib1*$^{-/-}$ bone marrow chimaeric mice (Fig. 4a). Mice lacking Trib1 throughout the whole body and in haematopoietic cells also developed glucose intolerance and insulin resistance on a HFD (Fig. 4b, c and Supplementary Fig. 20). In contrast, body weight did not differ significantly between wild-type and *Trib1*$^{-/-}$ bone marrow chimaeric mice fed a HFD (Supplementary Fig. 21). Whereas numbers of M1-type macrophages increased in both wild-type and *Trib1*$^{-/-}$ bone marrow chimaeric mice as well as mice lacking Trib1 in the whole body fed a HFD,

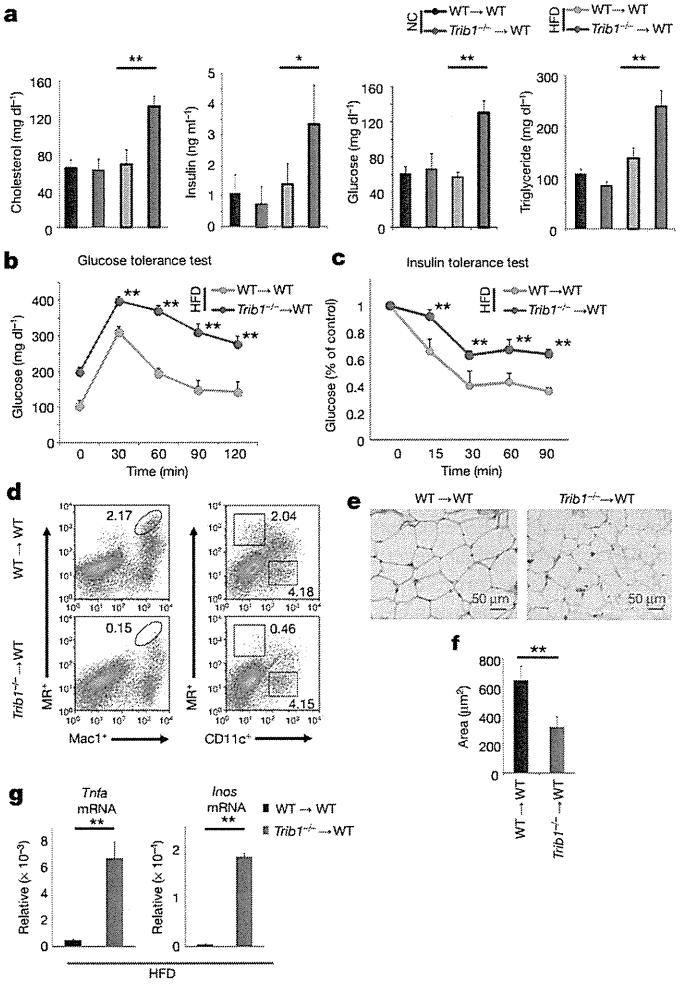

Figure 4 | Mice lacking Trib1 in haematopoietic cells develop exacerbated metabolic disorders on a high-fat diet. **a**, Serum samples were obtained from bone-marrow-transferred wild-type and *Trib1*$^{-/-}$ littermates fed normal chow (NC) or a high-fat diet (HFD). The concentrations of cholesterol, insulin, glucose and triglyceride were measured. Error bars indicate s.d. of duplicates. **b**, **c**, Fasting male bone-marrow-transferred wild-type and *Trib1*$^{-/-}$ littermates fed a HFD were challenged with intraperitoneal glucose (**b**) or insulin (**c**), and blood was sampled for glucose analyses at the indicated times. Data are mean s.d. of 5 samples. **d**, Flow cytometric analyses of haematopoietic cells from adipose tissues in wild-type and *Trib1*$^{-/-}$ mice fed a HFD. The expression levels of MR^+ and $Mac1^+$ tissue-resident macrophages are shown (left). The MR^+ and $CD11c^+$ macrophages in adipose tissue are also shown (right). **e**, **f**, Haematoxylin-and-eosin-stained images of paraffin-embedded epididymal adipose tissue sections are shown (**e**), and each area of adipocytes was measured (**f**). Scale bars, 50 μm. **g**, Total RNA was prepared from wild-type and *Trib1*$^{-/-}$ chimaeric mice fed a HFD. Error bars indicate s.d. of duplicates. The expression levels of mRNAs encoding the indicated genes were determined by quantitative PCR. Error bars indicate s.d. of duplicates. Statistical significance in **a**–**c**, **f**, **g** was determined using the Student's *t*-test. $*P < 0.05$; $**P < 0.01$.

M2-like macrophages were severely decreased in the absence of Trib1 (Fig. 4d and Supplementary Fig. 22). *Trib1*$^{-/-}$ chimaeric mice had smaller adipocytes on a HFD (Fig. 4e, f). Notably, *Tnf* and *Inos* mRNA were markedly augmented in *Trib1*$^{-/-}$ chimaeric mice (Fig. 4g). Taken together, these findings suggest that *Trib1*$^{-/-}$ bone marrow chimaeric mice develop metabolic disorders on a HFD through impaired lipid buffering caused by lipodystrophy.

Although we previously showed that Trib1 regulates C/EBPβ expression in thioglycollate-elicited macrophages[11], we found that M2-like macrophages were present in *Cebpb*$^{-/-}$ mice (data not shown). Thus, Trib1 seems to control different target proteins for degradation depending on the cell types and their differentiation stages. We previously showed that Jmjd3 is essential for M2-like macrophage differentiation in response to chitin administration and helminth infection[22,23]. However, Jmjd3 deficiency did not show any defect in tissue-resident M2-like macrophage generation (Supplementary Fig. 23). Reciprocally, Trib1 deficiency did not alter the activation of M2-like macrophages to chitin administration (Supplementary Fig. 24). It can be assumed that macrophage subtypes are more complex *in vivo*, although the precise classification of M2-type macrophages *in vivo* is yet to be clarified.

Chronic low-grade inflammation in adipose tissues is thought to have a central role in the exacerbation of metabolic disorders[24,25]. M1-type macrophages infiltrate into obese adipose tissues via MCP1, where they are activated in part by saturated fatty acids and cause low-grade inflammation by producing proinflammatory cytokines[26,27]. However, tissue-resident M2-like macrophages, which differentiate depending on the presence of Trib1 in the bone marrow, are subsequently activated in adipose tissues and the liver in response to IL-4 and IL-13 produced from eosinophils by a PPAR-γ- and PPAR-δ-dependent mechanism, respectively[21,28–30]. Further studies are required to clarify how tissue-resident M2-like macrophages maintain adipose tissue homeostasis. Trib1 was also essential for the development of eosinophils, nevertheless, we believe that Trib1 maintains adipose tissues by controlling M2-like macrophages, as supplementation of wild-type macrophages alone could rescue the lipodystrophy observed in *Trib1*$^{-/-}$ mice.

Mutations in TRIB1 have been implicated in metabolic disorders of humans. It is tempting to speculate that TRIB1 functions in a similar manner in humans and that other pathophysiologies, such as tumour progression, angiogenesis or tissue remodelling, are affected by these tissue-resident M2-like macrophages.

METHODS SUMMARY

Mice, reagents, cells and plasmids. Full details are provided in the Methods.

Colony-forming assay. Bone marrow cells (4×10^4) were seeded on 3.5-cm dishes and cultured for 7 days with Methocult (no. 3534; Stem Cell Technologies) containing SCF, IL-6 and IL-3 in the presence of 20 ng ml^{-1} M-CSF. The numbers of GFP-positive cells were counted for colony-forming assays or collected for real-time (q)PCR and western blotting.

Full Methods and any associated references are available in the online version of the paper.

Received 19 March 2012; accepted 22 January 2013.
Published online 20 March 2013.

1. Martinez, F. O., Helming, L. & Gordon, S. Alternative activation of macrophages: an immunologic functional perspective. *Annu. Rev. Immunol.* **27,** 451–483 (2009).
2. Biswas, S. K. & Mantovani, A. Macrophage plasticity and interaction with lymphocyte subsets: cancer as a paradigm. *Nature Immunol.* **11,** 889–896 (2010).
3. Mantovani, A. & Sica, A. Macrophages, innate immunity and cancer: balance, tolerance, and diversity. *Curr. Opin. Immunol.* **22,** 231–237 (2010).
4. Takeuchi, O. & Akira, S. Pattern recognition receptors and inflammation. *Cell* **140,** 805–820 (2010).
5. Medzhitov, R. Origin and physiological roles of inflammation. *Nature* **454,** 428–435 (2008).
6. Sica, A. & Mantovani, A. Macrophage plasticity and polarization: *in vivo* veritas. *J. Clin. Invest.* **122,** 787–795 (2012).
7. Yokoyama, T. *et al.* Trib1 links the MEK1/ERK pathway in myeloid leukemogenesis. *Blood* **116,** 2768–2775 (2010).
8. Varbo, A., Benn, M., Tybjaerg-Hansen, A., Grande, P. & Nordestgaard, B. G. TRIB1 and GCKR polymorphisms, lipid levels, and risk of ischemic heart disease in the general population. *Arterioscler. Thromb. Vasc. Biol.* **31,** 451–457 (2011).
9. Aung, L. H. *et al.* Association of the TRIB1 tribbles homolog 1 gene rs17321515 A>G polymorphism and serum lipid levels in the Mulao and Han populations. *Lipids Health Dis.* **10,** 230 (2011).
10. Chambers, J. C. *et al.* Genome-wide association study identifies loci influencing concentrations of liver enzymes in plasma. *Nature Genet.* **43,** 1131–1138 (2011).
11. Yamamoto, M. *et al.* Enhanced TLR-mediated NF-IL6 dependent gene expression by Trib1 deficiency. *J. Exp. Med.* **204,** 2233–2239 (2007).
12. Jin, G. *et al.* Trib1 and Evi1 cooperate with Hoxa and Meis1 in myeloid leukemogenesis. *Blood* **109,** 3998–4005 (2007).
13. Keeshan, K. *et al.* Tribbles homolog 2 inactivates C/EBPα and causes acute myelogenous leukemia. *Cancer Cell* **10,** 401–411 (2006).
14. Du, K., Herzig, S., Kulkarni, R. N. & Montminy, M. TRB3: A *tribbles* homolog that inhibits Akt/PKB activation by insulin in liver. *Science* **300,** 1574–1577 (2003).
15. Okamoto, H. *et al.* Genetic deletion of Trb3, the mammalian *Drosophila* tribbles homolog, displays normal hepatic insulin signaling and glucose homeostasis. *Diabetes* **56,** 1350–1356 (2007).
16. Kohyama, M. *et al.* Role for Spi-C in the development of red pulp macrophages and splenic iron homeostasis. *Nature* **457,** 318–321 (2009).
17. De Domenico, I., McVey Ward, D. & Kaplan, J. Regulation of iron acquisition and storage: consequences for iron-linked disorders. *Nature Rev. Mol. Cell Biol.* **9,** 72–81 (2008).
18. Hong, S., Skaist, A. M., Wheelan, S. J. & Friedman, A. D. AP-1 protein induction during monopoiesis favors C/EBP: AP-1 heterodimers over C/EBP homodimerization and stimulates FosB transcription. *J. Leukoc. Biol.* **90,** 643–651 (2011).
19. Odegaard, J. I. & Chawla, A. Alternative macrophage activation and metabolism. *Annu. Rev. Pathol.* **6,** 275–297 (2011).
20. Lumeng, C. N., Bodzin, J. L. & Saltiel, A. R. Obesity induces a phenotypic switch in adipose tissue macrophage polarization. *J. Clin. Invest.* **117,** 175–184 (2007).
21. Odegaard, J. I. *et al.* Macrophage-specific PPARγ controls alternative activation and improves insulin resistance. *Nature* **447,** 1116–1120 (2007).
22. Reese, T. A. *et al.* Chitin induces accumulation in tissue of innate immune cells associated with allergy. *Nature* **447,** 92–96 (2007).
23. Satoh, T. *et al.* The Jmjd3-Irf4 axis regulates M2 macrophage polarization and host responses against helminth infection. *Nature Immunol.* **11,** 936–944 (2010).
24. Chawla, A., Nguyen, K. D. & Goh, Y. P. Macrophage-mediated inflammation in metabolic disease. *Nature Rev. Immunol.* **11,** 738–749 (2011).
25. Gregor, M. F. & Hotamisligil, G. S. Inflammatory mechanisms in obesity. *Annu. Rev. Immunol.* **29,** 415–445 (2011).
26. Hotamisligil, G. S. Inflammation and metabolic disorders. *Nature* **444,** 860–867 (2006).
27. Wellen, K. E. & Hotamisligil, G. S. Obesity-induced inflammatory changes in adipose tissue. *J. Clin. Invest.* **112,** 1785–1788 (2003).
28. Wu, D. *et al.* Eosinophils sustain adipose alternatively activated macrophages associated with glucose homeostasis. *Science* **332,** 243–247 (2011).
29. Odegaard, J. I. *et al.* Alternative M2 activation of Kupffer cells by PPARδ ameliorates obesity-induced insulin resistance. *Cell Metab.* **7,** 496–507 (2008).
30. Ricardo-Gonzalez, R. R. *et al.* IL-4/STAT6 immune axis regulates peripheral nutrient metabolism and insulin sensitivity. *Proc. Natl Acad. Sci. USA* **107,** 22617–22622 (2010).

Supplementary Information is available in the online version of the paper.

Acknowledgements We thank I. Shimomura and Y. Miyata for providing us with the key protocols for the metabolic experiments; T. Kitamura for providing the PlatE cells; M. Higa, H. Tanaka, N. Miyamoto, K. Miura, D. Ori, T. Uehata and K. Kuniyoshi for assistance with the experiments; and T. Kawai, S. Uematsu, T. Saitoh and Y. Kumagai for discussions. We also thank E. Kamada and M. Kageyama for secretarial assistance, and N. Umano, Y. Matsumoto and M. Kumagai for technical assistance. This work was supported by the Special Coordination Funds of the Japanese Ministry of Education, Culture, Sports, Science and Technology, and the Ministry of Health, Labour and Welfare in Japan, the Japan Society for the Promotion of Science through the Funding Program for World-Leading Innovative R&D on Science and Technology (FIRST Program).

Author Contributions T.S. designed and performed the experiments and wrote the manuscript. H.K., H.N. and N. Takakura performed the colony-forming assays. M.Y. generated the *Trib1*$^{-/-}$, *Trib2*$^{-/-}$ and *Trib3*$^{-/-}$ mice. N. Takemura helped with experiments. K.N. performed microarray analysis. Y.Y. performed the MRI experiments. E.M. performed the histological analyses. O.T. and S.A. designed experiments and wrote the manuscript. S.A. supervised the project.

Author Information Data have been deposited in the GEO under accession number GSE43563. Reprints and permissions information is available at www.nature.com/reprints. The authors declare no competing financial interests. Readers are welcome to comment on the online version of the paper. Correspondence and requests for materials should be addressed to S.A. (sakira@biken.osaka-u.ac.jp).

METHODS

Mice, cells and reagents. *Trib1*$^{-/-}$ mice were generated as described previously[11]. Antibodies for flow cytometry were purchased from commercial sources as follows: anti-F4/80-FITC (BM8; BioLegend); anti-Mac1-PerCP Cy5.5 (M1/70; BD Biosciences); anti-Ly6C-FITC (AL-21; BD Biosciences); anti-Siglec-F-PE (E50-2446; BD Biosciences); anti-CCR3-APC (83103; BD Biosciences); anti-MR-Alexa 488 (MR5D3; BioLegend); and anti-CD11c-Brilliant bright (N418; BioLegend). Antibodies and reagents for histochemical analysis were purchased from commercial sources as follows: biotinylated anti-F4/80 (eBioscience), anti-MOMA-1 (Abcam), Alexa 488-conjugated anti-B220 (BD Pharmingen) and streptavidin-Alexa594 (Invitrogen). Antibodies for western blotting were purchased as follows: anti-C/EBPα (no. 2295; Cell Signaling Technology); anti-C/EBPβ (no. E298; Millipore); anti-C/EBPδ (no. 2318; CST); anti-C/EBPε (no. sc-158; Santa Cruz Biotechnology); and anti-actin (no. sc-1615; Santa Cruz Biotechnology). The probes for quantitative PCR were purchased from Lifescience Japan.

Generation of *Trib2*$^{-/-}$ and *Trib3*$^{-/-}$ mice. The *Trib2* and *Trib3* genes were isolated from genomic DNA extracted from embryonic stem (ES) cells (GSI-I) by PCR. The targeting vectors were constructed by replacing a 2-kilobase (kb) fragment encoding the *Trib2* open reading frame (exon 2) and replacing a 2.5-kb fragment encoding the *Trib3* open reading frame (exons 2–3) with a neomycin-resistance gene cassette (*neo*), and inserting herpes simplex virus thymidine kinase (HSV-TK) driven by the PGK promoter into the genomic fragment for negative selection. After each targeting vector was transfected into ES cells, G418 and ganciclovir double-resistant colonies were selected and screened by PCR, and recombination was further confirmed by Southern blotting. The homologous recombinant clones were individually microinjected into blastocysts derived from C57BL/6 mice and then transferred to pseudopregnant females. Mating of chimaeric male mice with C57BL/6 female mice resulted in the transmission of each mutant allele to the germ line. The resulting *Trib2*$^{+/-}$ and *Trib3*$^{+/-}$ mice were interbred to generate *Trib2*$^{-/-}$ *and Trib3*$^{-/-}$ mice, respectively. All animal experiments were performed with approval from the Animal Research Committee of the Research Institute for Microbial Diseases (Osaka University).

Construction of expression plasmids and shRNA vectors. *Trib1* and *Cebpa* cDNAs were obtained by PCR from a mouse cDNA library. Full-length or mutated *Trib1* cDNAs were cloned into the pLZR-cmv-ires-GFP vector for retrovirus production. For shRNA experiments, the following oligonucleotides were used to target mouse C/EBPα: cebpa-8 dn, 5′-gatccGTCGTATGTATTATATCTATA TTCAAGAGATATAGATATAATACATACGACTTTTTTACGCGTg-3′ and cebpa-8 up, 5′-aattcACGCGTAAAAAAGTCGTATGTATTATATCTATATC TCTTGAATATAGATATAATACATACGACg-3′; cebpa-12 dn, 5′-gatccATCC GATATCAACACTTGTATTTCAAGAGAATACAAGTGTTGATATCGGATT TTTTTACGCGTg-3′ and cebpa-12 up, 5′-aattcACGCGTAAAAAAATCCGA TATCAACACTTGTATTCTCTTGAAATACAAGTGTTGATATCGGATg-3′. The oligonucleotides were annealed and ligated with the RNAi-ready pSIREN-RetroQ-zsGreen vector (Takara). Lowercase letters indicate the site of restriction enzyme.

Colony-forming assay. Bone marrow cells (4×10^4) were seeded on 3.5-cm dishes and cultured for 7 days with Methocult (no. 3534; Stem Cell Technologies) containing SCF, IL-6 and IL-3 in the presence of 20 ng ml^{-1} M-CSF. The numbers of GFP-positive cells were counted for colony-forming assays or collected for real-time (q)PCR and western blotting.

Assessment of glucose, insulin and NEFA levels and glucose and insulin sensitivity *in vivo*. Serum insulin levels were determined by ELISA (Morinaga Institute of Biological Science Inc.). Serum glucose, NEFA and cholesterol levels were measured with enzymatic kits (WAKO Chemicals). Intraperitoneal glucose tolerance tests were performed on 16 h fasted mice injected intraperitoneally with D-glucose (1.5 mg g^{-1} body weight). Serum glucose levels were measured immediately before and 30, 60, 90 and 120 min after the D-glucose injection. Intraperitoneal insulin tolerance tests were performed on 4 h fasted mice injected intraperitoneally with insulin (1 mU g^{-1} body weight). Serum glucose levels were measured immediately before and 15, 30, 60 and 90 min after the insulin injection.

Lipolysis assay. *In vivo* lipolysis assays were performed on 4 h fasted mice. Blood was collected from orbital veins, and the serum glycerol and NEFA concentrations were measured.

Quantitative PCR analysis. Total RNA was isolated using Trizol (Invitrogen) and subjected to reverse transcription with ReverTra Ace (Toyobo) according to the manufacturer's instructions. For quantitative PCR, cDNA fragments were amplified using real-time PCR Master Mix (Toyobo). Fluorescence from the TaqMan probe for each cytokine was detected using a 7500 Real-time PCR System (Applied Biosystems). To determine the relative induction of each cytokine mRNA in response to various stimuli, the mRNA expression level of each gene was normalized to the 18S rRNA expression level. The experiments were repeated at least twice.

Assay ID numbers are: *Arg1*, Mm00475988_m1, *Ym1*, Mm00657889_mH, *Fizz1*, Mm00445109_m1, *MR*, Mm00485148_m1; *Trib1*, Mm00454875_m1; *Trib2*, Mm0045 4876_ml; *Trib3*, Mm00454879_m1; *Acaca*, Mm01304277_m1; *Fasn*, Mm00662319_m1; *Acsl1*, Mm00484217_m1; *PParg*, Mm01184322_m1; *Cebpa*, Mm00514283_s1; *Cebpb*, Mm00843434_s1; *Cebpd*, Mm00786711_s1; *Il10*, Mm00439614_m1; *Tnfa*, Mm99999068_m1; *Inos*, Mm00440485_m1.

Immunoblot analysis. Bone marrow cells were collected and red blood cells were lysed using red blood cell lysis buffer (Invitrogen). After two washes with MACS buffer, lineage-negative cells were collected by MACS sorting using anti-CD3, anti-CD19, anti-B220, anti-Ter119, anti-Gr1, anti-DX5, anti-Mac1 and anti-CD11c MACS beads (Miltenyi Biotec). The lineage-negative cells were lysed with lysis buffer (20 mM Tris-HCl, pH 7.5, 150 mM NaCl, 1 mM EDTA, 1% NP40) containing Complete Protease Inhibitor Cocktail (Roche). The cell lysates were separated by standard SDS–PAGE and analysed by immunoblotting. Antibodies against the following proteins were used: C/EBPα, C/EBPβ, C/EBPδ, C/EBPε and actin. The Luminata Forte Western HRP Substrate (Millipore) was used for the development of positive signals.

Flow cytometry. Cell suspensions were prepared by sieving and gentle pipetting. After washing with ice-cold FACS buffer (0.5% BSA and 2 mM EDTA in PBS, pH 7.2), the cells were incubated with antibodies for 15 min and washed twice with FACS buffer. Data were acquired using a FACSCalibur flow cytometer (BD), and analysed by FlowJo software (Tree Star).

Retroviral preparation. Retroviruses were produced using PlatE packaging cells or transfected with various plasmids. Bone marrow cells were transduced with the retroviral supernatants (supplemented with polybrene (Millipore)) twice. After the second transduction, the cells were washed twice and re-suspended in RPMI medium.

Magnetic resonance imaging (MRI). An 11.7 T MRI scanner (AVANCE-II 500 WB; Bruker BioSpin) was used to acquire *in vivo* mouse images. Mice were anaesthetized with 1.0–1.5% isoflurane during the MRI procedures. We used a T_2-weighted imaging sequence (RARE) with the following parameters: field of view, 2.5 × 2.5 cm; matrix size, 256 × 256; slice thickness, 0.5 mm; repetition time, 5,000 ms; echo time, 25.2 ms; average, 4; scan time, 5 min.

Histochemical analysis. Frozen 6-μm tissue sections were fixed in 4% paraformaldehyde and blocked with 5% BSA (Invitrogen). For Perl's Prussian blue staining, tissues were fixed with 4% paraformaldehyde in phosphate buffer (pH 7.0), embedded in paraffin and stained with Perl's Prussian blue.

Generation of bone-marrow-transferred chimaeric mice. Bone marrow cells were prepared from wild-type and *Trib1*$^{-/-}$ mice, and intravenously injected into lethally irradiated CD45.1 C57BL/6 mice, wild-type and *Trib1*$^{-/-}$ mice. The chimaeric mice were administered neomycin (Sigma) and polymyxin B (Sigma) in their drinking water for 8 weeks. The mice were analysed for at least 12 weeks after reconstitution. More than 90% of splenocytes from the chimaeric mice were CD45.2^{+}.

Mouse SVF and MAF isolation. Epididymal fat pads from male mice fed a normal or HFD were excised and minced in Krebs-Ringer-bicarbonate-HEPES buffer (KRBH: 120 mM NaCl, 4 mM KH_2PO_4, 1 mM $MgSO_4$, 1 mM $CaCl_2$, 10 mM $NaHCO_3$, 30 mM HEPES, 20 μM adenosine (Sigma), 4% BSA). The tissues were then digested with 1 mg ml^{-1} collagenase type II (Sigma) in PBS at 37 °C for 30 min with gentle shaking and filtered through a 100-mm filter. In SVF preparations, the digested cells were separated by centrifugation at 700*g* for 5 min. In MAF preparations, the digested cells were separated by centrifugation at 300*g* for 5 min. The resulting cells were washed twice with KRBH buffer before use in experiments.

Metabolic measurements. Serum insulin levels were determined by ELISA (Morinaga Institute of Biological Science Inc.). Serum glucose, NEFA and cholesterol levels were measured with enzymatic kits (WAKO Chemicals). Intraperitoneal glucose tolerance tests were performed on 16 h fasted mice injected intraperitoneally with D-glucose (1.5 mg g^{-1} body weight). Serum glucose levels were measured immediately before administration and 30, 60, 90 and 120 min after the D-glucose injection.

Lipolysis assay. *In vivo* lipolysis assays were performed on 4 h fasted mice. Blood was collected from orbital veins, and the serum glycerol and NEFA concentrations were measured. For *ex vivo* assays, adipocytes were isolated from epididymal pads using collagenase, washed twice, re-suspended in Krebs-Ringer buffer at 5×10^5 cells ml^{-1} and incubated with shaking for the specified times. The glycerol and NEFA concentrations were measured in the supernatants.

Microarray analysis. Total RNA was isolated from wild-type and *Trib1*$^{-/-}$ GMP and MDP using TRIzol RNA isolation kit (Invitrogen) and further purified using an RNeasy kit (Qiagen). Biotinylated cDNA was synthesized from 100 ng total RNA with the Ovation biotin RNA amplification and labelling systems (Nugen) according to the manufacturer's protocol. The product was purified using an DyeEx 2.0 spin kit (QIAGEN), fragmented, and hybridized to Affymetrix mouse

expression array A430 2.0 microarray chips, according to the manufacturer's protocol (Affymetrix). Staining, washing and scanning of Affymetrix mouse Genome 430 2.0 microarray chips was done following the manufacturer's instructions. Robust multichip average (RMA) expression values were calculated using R and the Bioconductor affy package. For each probe the changes in expression between wild-type and *Trib1*$^{-/-}$ samples were defined as the difference between $\log_2$ values for wild-type and *Trib1*$^{-/-}$ cells. Genes were assigned the values of their corresponding probe(s). In cases where a gene was associated with multiple probes the average value was taken.

Statistical analysis. The statistical significance of differences between values was calculated using the two-tailed Student's *t*-test. Values of $^{*}P < 0.05$, $^{**}P < 0.01$ were considered to indicate statistical significance.

PLOS ONE

An Angiogenic Role for Adrenomedullin in Choroidal Neovascularization

Susumu Sakimoto[1,2], Hiroyasu Kidoya[1], Motohiro Kamei[2], Hisamichi Naito[1], Daishi Yamakawa[1], Hirokazu Sakaguchi[2], Taku Wakabayashi[1,2], Kohji Nishida[2], Nobuyuki Takakura[1,3]*

1 Department of Signal Transduction, Research Institute for Microbial Diseases, Osaka University, Suita, Osaka, Japan, **2** Department of Ophthalmology, Osaka University Graduate School of Medicine, Suita, Osaka, Japan, **3** JST(Japan Science and Technology Agency), CREST, Tokyo, Japan

Abstract

Purpose: Adrenomedullin (ADM) has been shown to take part in physiological and pathological angiogenesis. The purpose of this study was to investigate whether ADM signaling is involved in choroidal neovascularization (CNV) using a mouse model.

Methods and Results: CNV was induced by laser photocoagulation in 8-week-old C57BL/6 mice. ADM mRNA expression significantly increased following treatment, peaking 4 days thereafter. The expression of ADM receptor (ADM-R) components (CRLR, RAMP2 and RAMP 3) was higher in $CD31^{+}CD45^{-}$ endothelial cells (ECs) than $CD31^{-}CD45^{-}$ non-ECs. Inflammatory stimulation upregulated the expression of ADM not only in cell lines but also in cells in primary cultures of the choroid/retinal pigment epithelium complex. Supernatants from TNFα-treated macrophage cell lines potentiated the proliferation of ECs and this was partially suppressed by an ADM antagonist, ADM (22–52). Intravitreous injection of ADM (22–52) or ADM neutralizing monoclonal antibody (mAb) after laser treatment significantly reduced the size of CNV compared with vehicle-treated controls ($p<0.01$).

Conclusions: ADM signaling is involved in laser-induced CNV formation, because both an ADM antagonist and ADM mAb significantly inhibited it. Suppression of ADM signaling might be a valuable alternative treatment for CNV associated with age-related macular degeneration.

Citation: Sakimoto S, Kidoya H, Kamei M, Naito H, Yamakawa D, et al. (2013) An Angiogenic Role for Adrenomedullin in Choroidal Neovascularization. PLoS ONE 8(3): e58096. doi:10.1371/journal.pone.0058096

Editor: Tailoi Chan-Ling, University of Sydney, Australia

Received March 30, 2012; **Accepted** February 3, 2013; **Published** March 8, 2013

Funding: This work was supported by a grant from the Ministry of Education, Science, Sports, and Culture of Japan. The funders had no role in study design, data collection and analysis, decision to publish.

Competing Interests: The authors have declared that no competing interests exist.

* E-mail: ntakaku@biken.osaka-u.ac.jp

Introduction

Aberrant angiogenesis occurs under numerous pathological conditions, such as cancer, rheumatoid arthritis, psoriasis and many ocular diseases. Age-related macular degeneration (AMD) is the leading cause of vision loss in elderly persons in developed countries. Patients with severe vision loss are often affected by wet AMD [1] the central pathologic features of which are recognized as choroidal neovascularization (CNV), induced by a complex pathogenic process whereby new blood vessels are generated from the choriocapillaris beneath the retina. CNV-associated vessels tend to leak and bleed, thereby severely affecting the neural tissue of the macula.

Genetic variation in complement factor genes in AMD patients suggests inflammatory processes as a trigger of drusen formation which is a hallmark of this disease. Moreover, infiltration of inflammatory cells such as macrophages which produce various angiogenic factors could support neovessel formation from the choriocappillaris directly and indirectly [2,3,4,5].

Adrenomedullin (ADM), identified as a potent vasodilator with wide tissue distribution, is a multifunctional 52 amino acid peptide activating heterodimeric receptors composed of a seven transmembrane (7TM) G-protein-coupled receptor (GPCR) calcitonin-receptor-like receptor (CRLR, now known as CL) [6] and receptor activity-modifying proteins (RAMPs) [7]. ADM is also thought to play a critical role in forming blood vessels, with functions including regulation of vascular stability under both physiological and pathological conditions [8–10]. Gene targeting analysis in mice showed that global deletion of the ADM gene results in embryonic lethality at E13.5 caused by vascular abnormalities [10].

Expression of ADM is regulated by hypoxia, growth factors and inflammation [6,8]. Moreover, accumulating evidence for the involvement of ADM in tumor angiogenesis has demonstrated that inhibition of ADM function by neutralizing antibody or the ADM antagonist ADM (22–52) inhibits tumor growth in xenograft models [11,12,13]. In vascular endothelial cells (ECs), activation of phosphatidylinositol 3′ kinase (PI3K/Akt), mitogen-activated protein kinase (MAPK) and focal adhesion kinase (p125FAK) plays a role in ADM-induced angiogenesis [8,14,15]. The level of ADM expression in tumors correlates with vascular density in patients [16] and ADM-heterozygous knockout mice have reduced neovascularization in a tumor xenograft model [9].

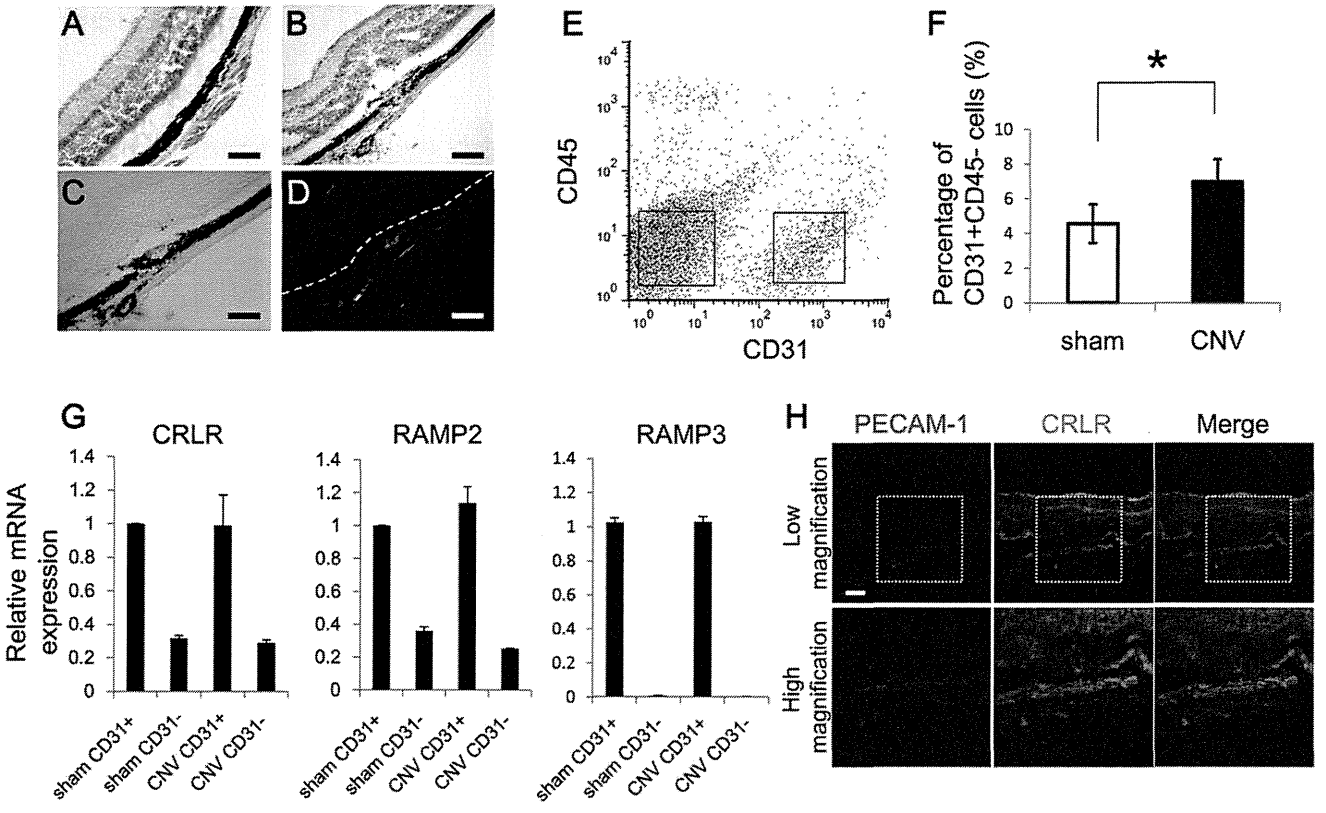

Figure 1. Expression of ADM receptors in choroidal ECs. (A, B) Hematoxylin-eosin-stained light micrograph of normal eye (A) and CNV lesion 7 days after laser treatment (B). Bar, 100 μm. (C) Light micrograph of serial sections of (B). Bar, 100 μm. (D) Immunohistochemistry of (C) with anti-PECAM-1/CD31 antibody. Dotted line indicates the borderline between the neural retina and RPE. Because the CNV lesion did not invade into the retina in this model, we could sort the ECs not from nerural retina but from CNV lesions and choroidal tissue in the following flow cytometry experiments. Bar, 100 μm. (E) Flow cytometric analysis of choroidal ECs from wild-type mice. $CD31^{+}CD45^{-}$ cells gated on the right are designated as ECs. (F) Quantitative evaluation of the percentage of choroidal EC 7 days after laser treatment. The number was calculated per cell total ($n = \geq 5$, $^{*}P<0.05$). (G) qRT–PCR analysis of ADM receptor component expression in choroidal ECs. The value in $CD31^{+}CD45^{-}$ECs was compared with that in $CD31^{-}CD45^{-}$ non-ECs sorted as gated in (A). Note that the expression level of ADM receptors is not significantly different between ECs and non-ECs in both sham-operated mice (sham) and laser-irradiated CNV mice (CNV). (H) Immunostaining of the CNV 7 days after laser treatment with anti-PECAM-1 (red) and anti-CRLR (green) antibody. High maginification indicate the dotted box in Low magnification. Bar, 100 μm.
doi:10.1371/journal.pone.0058096.g001

However, it is poorly understood whether ADM could be an effector in other disease models, especially in ocular neovascularization. Therefore, here we investigate whether ADM has a role in proangiogenesis in laser-induced CNV, which is widely accepted as a mammalian AMD model, and have attempted to characterize mechanisms of ADM signaling in CNV formation.

Materials and Methods

Animals

All experiments were conducted under the applicable laws and guidelines for the care and use of laboratory animals in the Research Institute for Microbial Diseases, Osaka University, approved by the Animal Experiment Committee of the Research Institute for Microbial Disease, Osaka University.

Laser-induced CNV and Drug Treatment

Laser photocoagulation (514 nm Argon laser, 150 mW, 50 ms duration, 50 mm spot size; Ultima 2000 SE, Lumenis/Coherent) was performed bilaterally in each 8-week-old wild-type C57BL/6 mouse. A total of 6 laser spots per eye were created in a standard fashion around the optic nerve using a slit lamp delivery system (Carl Zeiss, Germany) and using a cover slip as a contact lens. Only burns that produced a bubble, indicating rupture of the Bruch membrane, were included in the study. Eyes merely touched with a cover slip acted as sham-operated controls. Immediately after laser photocoagulation, mice were randomized into several groups and received intravitreal injections of 1 μl ADM (22–52) (10 μM or 100 μM), ADM (200 μM) (Peptide Institute, Osaka, Japan), SU1498 (10 μM) [17], ADM monoclonal antibody (1.45 mg/ml) (provided by Diagnostic Science Division, Shionogi & Co., Ltd.) or vehicle (PBS). The same treatment was performed 3 days after photocoagulation in the same fashion. Intravitreal injection was performed with the FemtoJet Microinjector System (Eppendorf, Germany) under a high magnification stereomicroscope (Leica M125, Germany). Eyes were enucleated and fixed for immunohistochemistry 7 days after photocoagulation. We used 16 mice and 16 choroidal flatmounts in ADM antagonist experiments, 8 mice and 8 flatmounts in experiments using combination treatment with ADM antagonist and VEGF inhibitor, and 10 mice and 10 flatmounts in ADM mAb experiments.

Measurement of Laser-induced CNV Size

On day 7 after laser photocoagulation, the sizes of CNV lesions were measured on RPE-choroid flat mounts as described pre-

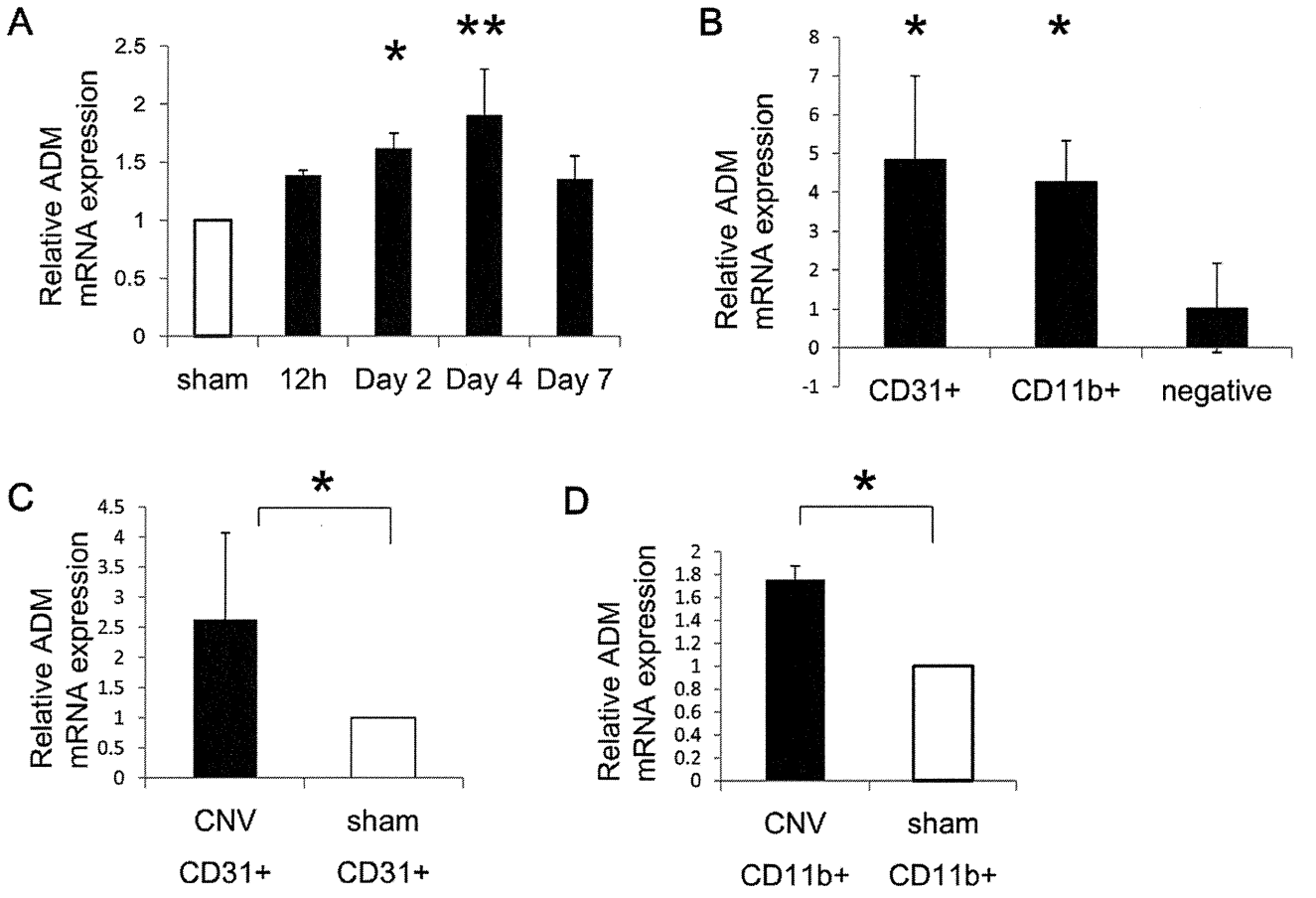

Figure 2. ADM expression after laser treatment. (A) Time course ADM mRNA expression by qRT–PCR analysis in the RPE/choroid complex after laser treatment. Results are shown as fold-increase in comparison with RPE/choroid complexes from sham-operated eyes. (B) qRT–PCR analysis of ADM mRNA expression in sorted CD31$^+$ cells (EC-enriched cell population), CD11b$^+$ cells (monocyte/macrophage lineage cells) and cells negative for either CD31 or CD11b (non-EC, non-monocyte/macrophage lineage fraction) 3 days after laser treatment ($n \geq 5$). (C) qRT–PCR analysis of ADM mRNA expression in sorted CD31$^+$ cells after laser treatment (CNV) compared to sham-treated eyes (sham). ($n \geq 5$, *$P<0.05$) (D) qRT–PCR analysis of ADM mRNA expression in sorted CD11b$^+$ cells after laser treatment compared to sham-treated eyes. ($n \geq 5$, *$P<0.05$).
doi:10.1371/journal.pone.0058096.g002

viously [18]. Image J for Windows (NIH, Bethesda, Maryland) analysis software was used to measure the area of CNV, with the operator blinded with respect to treatment groups.

Flow Cytometry (Analysis and Cell Sorting)

Procedures for cell preparation and staining were as previously reported [19]. Briefly, eyes from at least 5 mice which were laser coagulated or not were extracted and the RPE-choroid complex were gently scraped off the sclera. The RPE-complex was digested with collagenase (Wako, Osaka, Japan), and type II collagenase (Worthington Biochemical Corp., Lakewood, New Jersey) at 37°C. The digested tissue was passed through 40-μm filters to yield single cell suspensions. Cell surface antigen staining was performed as described previously [20]. Anti-CD45, -CD31, -CD11b (Pharmingen, BD Biosciences) mAbs were used for immunofluorescence staining. The stained cells were analyzed and sorted using a FACSAria flow cytometer (BD) with FlowJo (TreeStar) software. Dead cells were excluded from the analyses using the 2D profile of forward versus side scatter.

Quantitative Reverse-transcription Real-time PCR (qRT-PCR)

For RNA extraction, we used at least 5 mice in each group for sorted cells as indicated above. For analysis of ADM mRNA expression in RPE/choroid complexes, we used 2 mice per day. RNA was extracted from cells using an RNeasy Mini Kit (Qiagen), and cDNA was generated using reverse transcriptase from the ExScript RT reagent Kit (Perfect Real Time) (Takara). Real-time PCR was performed using a Stratagene Mx3000P (Stratagene, La Jolla, CA). Polymerase chain reaction (PCR) was performed on cDNA using specific primers following; mouse CRLR, 5′-ACC TGC ACA CAC TCA TCG TG-3′ and 5′-TGA TCC AGC AAT TGT CGT TG-3′; mouse RAMP2, 5′-CTG AGG ACA GCC TTG TGT CA-3′ and 5′-AAG TCC AGT TGC ACC AGT CC-3′; mouse RAMP3, 5′-AAG GTG GCT GTC TGG AAG TG-3′ and 5′-TGA TGT TGG TCT CCA TCT CG′; mouse ADM, 5′- GAC TCG CTG ATG AGA CGA CA-3′ and 5′- GAA CCC TGG TTC ATG CTC TG′; mouse GAPDH, 5′-TGG CAA AGT GGA GAT TGT TGC C-3′ and 5′- AAG ATG GTG ATG GGC TTC CCG-3′; human ADM, 5′- ATG AAG GGT GCC TCT CGA A-3′ and 5′- CCC TGG AAG TTG TTC ATG C-3′; human GAPDH, 5′- GAA GGT GAA GGT CGG AGT C-3′ and 5′- GAA GAT GGT GAT GGG ATT TC-3′.

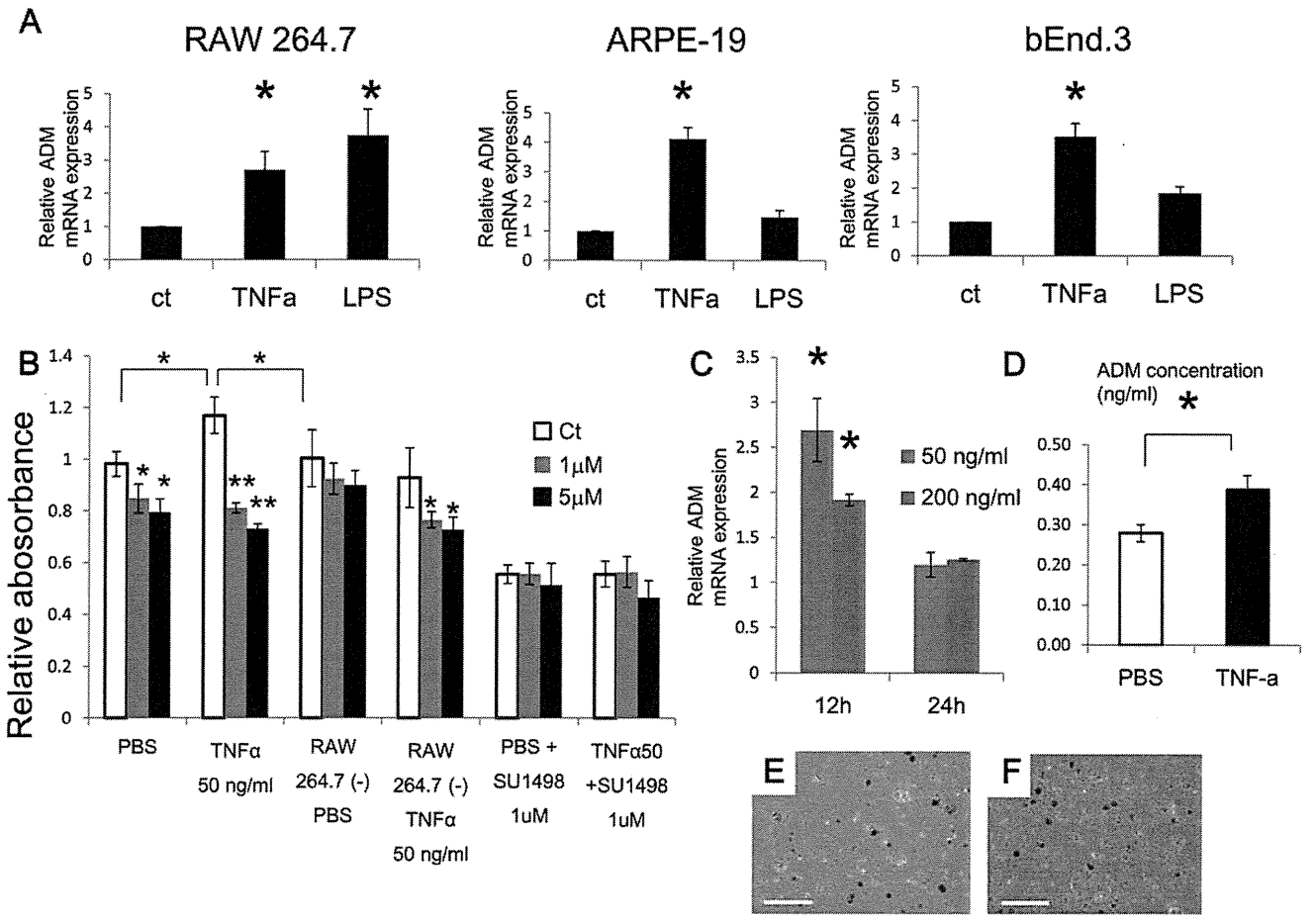

Figure 3. In vitro effect of an ADM antagonist. (A) qRT–PCR analysis of ADM mRNA expression after 12 hr TNF-α or LPS stimulation of cells, as indicated (n = 3, *P<0.01). (B) EC proliferation assay using bEND.3 which was incubated with or without supernatant from TNF-α-stimulated RAW 264.7 in the presence or absence of the ADM antagonist ADM (22–52). The white bar indicates the PBS group, gray indicates the 1 μM ADM (22–52) group and black the 5 μM ADM (22–52) group. ECs in all groups were incubated with supernatant from RAW 264.7 cells except for RAW 264.7 (-) groups (culture medium without supernatant of RAW 264.7 cells). 1 μM SU1498 was added to indicated groups (n = 3, **P<0.01, *P<0.05). (C) qRT–PCR analysis of ADM mRNA expression after 12 and 24 hr TNF-α stimulation of primary RPE/choroid cultures (n = 3, *P<0.05). (D) ELISA of secreted ADM from primary RPE/choroid cultures after stimulation with 50 ng/ml TNF-α or culture with PBS alone (*P<0.05) (E, F) Appearance of primary RPE/choroid cultures after stimulation with PBS (E) or 50 ng/ml TNF-α(F). Scale bar: 100 μm.
doi:10.1371/journal.pone.0058096.g003

Expression level of the target gene was normalized to the GAPDH level in each sample.

In vitro Assays

We examined the in vitro effect of ADM on inflammatory responses of 3 major cell types associated with CNV formation, i.e., microvascular ECs, macrophages, and RPE cells, using the murine cell lines bEnd3, RAW264.7, and the human cell line ARPE-19, respectively. ARPE19 cells were purchased from the American Type Culture Collection (ATCC, Manassas, VA). Cells were cultured in six-well plates for 12 hours in DMEM (Sigma, ATCC and Nikken, respectively). After 4 hours serum starvation using 0.5% fetal bovine serum (FBS), cells were stimulated with tumor necrosis factor (TNF)-α (PeproTech, 50 ng/mL) or lipopolysaccharide (LPS; Wako, 10 μg/mL). After a 12 hour incubation, cell lysate from each line, and the supernatants from cultures of RAW264.7 cells, were processed for real-time RT PCR and EC proliferation assays, respectively. ECs (bEnd3) which were incubated for an additional 4 hours with supernatant plus 1 μM or 5 μM ADM (22–52), or PBS, were quantified using Cell-counting kit-8 (DOJINDO) according to the supplier's protocol. 1 μM SU1498 was added to the supernatant in some experiments. Dose-response model assessing the toxicity of ADM (22–52) was also performed using same kit after 24 hour incubation of ADM inhibitor at indicated concentration. Absorbance was then measured at 490 nm, and at 630 nm as reference, with a Microplate Reader 550 (Bio-Rad Laboratories). Primary culture of RPE/choroid complexes was performed using cells dissected from 8-week-old wild-type C57BL/6 mice. Tissues were dissociated with trypsin, resuspended in DMEM containing 20% FBS and then plated on laminin-coated 24-well plates at a density of a tissue from1 mouse/well and incubated at 37°C, 5% CO_2 for 24 h before 4 hours serum starvation with 0.5% FBS. After 12 hours TNF-α treatment, tissues were collected and immediately washed with PBS before RNA extraction. For ELISA, after seeding the primary culture, we cultured for 24 hours as indicated above, then serum-starved for 4 hours in DMEM without FBS before TNF-α stimulation. We stimulated cells with 50 ng/ml TNF-α for 24 hours without FBS. We used an ADM detection kit (Phoenix Pharmaceuticals) according to the supplier's protocol.

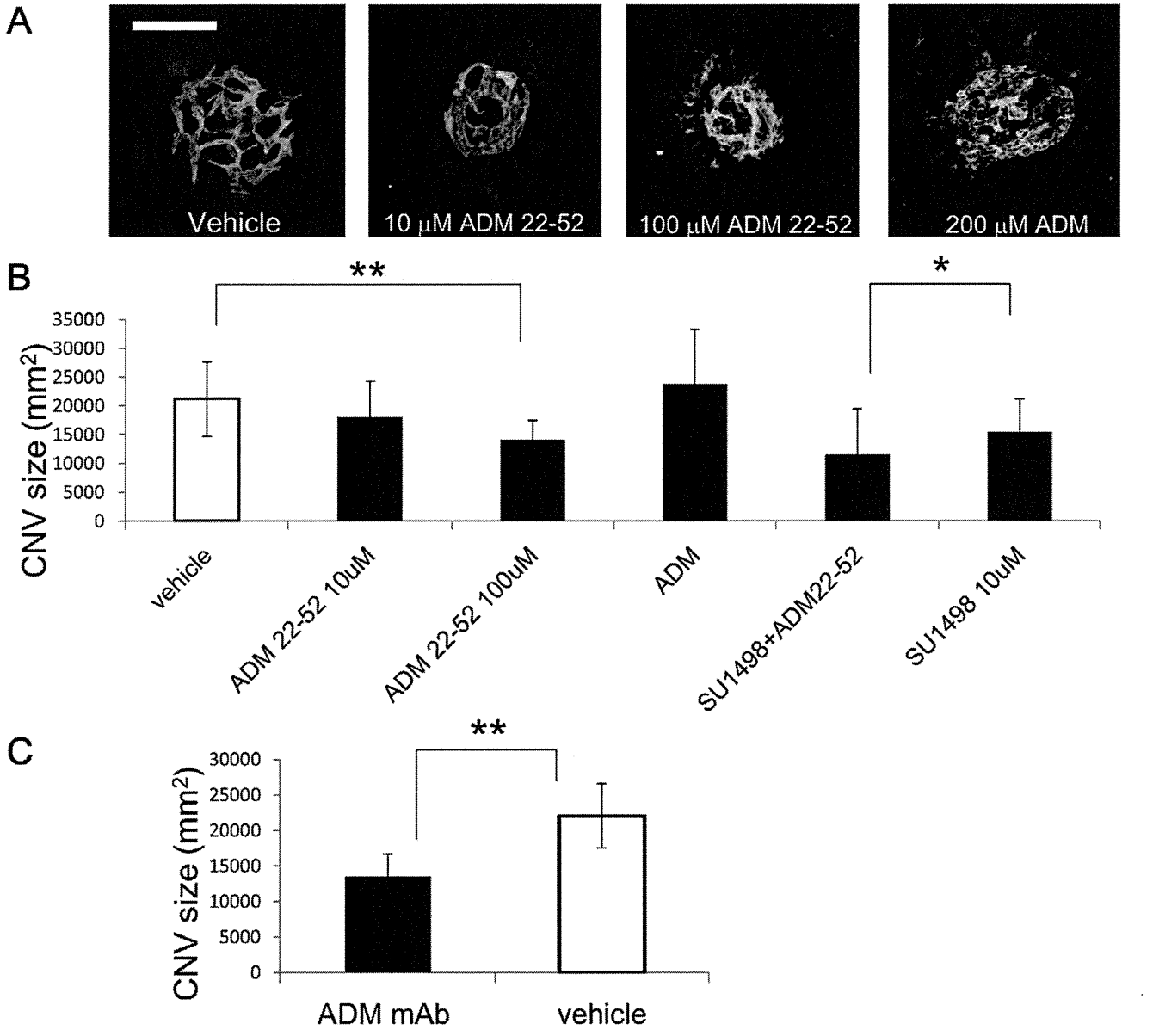

Figure 4. Suppression of CNV in mice by blocking ADM. (A) Flat-mount immunofluorescence staining with anti-PECAM-1/CD31 antibody in the choroid after vehicle, ADM (22–52) or recombinant ADM treatment. Scale bar: 100 μm. (B) Quantitative analysis of CNV size as revealed in (A). (n = 16, **P<0.01) and quantitative analysis of CNV size after treatment with 10 μM SU1498 with or without 100 μM ADM (22–52) (n = 8, *P<0.05). (C) Quantitative analysis of CNV size treated with ADM mAb compared to vehicle. (n = 10, **P<0.01). Error bars indicate mean ± s.d.
doi:10.1371/journal.pone.0058096.g004

Immunohistochemistry

The procedure for tissue preparation and staining was as previously reported [21]. For immunohistochemistry, biotin-conjugated anti-CD31 antibody (BD Biosciences, 1:200) was used for staining and anti-rat IgG Alexa Fluor 488 (Invitrogen, 1:300) as the secondary antibody. Samples were visualized using DM5500B (Leica) and confocal microscopy (TCS/SP5, Leica). Images were acquired with a DFC 500 digital camera (Leica) and processed with the Leica application suite (Leica) and Adobe Photoshop CS3 software (Adobe systems). All images shown are representative of more than 6 independent experiments.

Statistical Analysis

All data are presented as mean ± standard error of the mean (SEM). For statistical analysis, the statcel 2 software package (OMS) was used. In experiments involving qRT-PCR and CNV suppression with ADM mAb, we used two-sided Student's t-test to compare two groups (except for expression of ADM mRNA after CNV induction).We used analysis of variance performed on all data followed by Tukey–Kramer multiple comparison testing in qRT-PCR experiments for expression of ADM mRNA after CNV induction, EC proliferation assays using bEND.3 and for experiments on CNV suppression with ADM and VEGF antagonists. A probability value of less than 0.05 was considered statistically significant.

Results

To elucidate the involvement of ADM signaling in CNV, we first investigated the expression of the ADM receptor in choroidal vascular ECs in the CNV model. After we confirmed that CNV did not invade retinal tissue (Fig. 1A–D), $CD31^+CD45^-$ ECs in the RPE-choroid complex were analyzed by flow cytometry (Fig. 1E) and their number was calculated as a percentage of a total of 5×10^4 choroid/RPE complex cells 7 days after laser induction. We confirmed that the number of ECs increases after induction of CNV in laser-treated eyes (6.96% of total cells) compared to control eyes (4.57% of total cells) (Fig. 1F). There was no change in the number of $CD31^+$ $CD45^+$ or $CD31^-CD45^+$ cells; however, CD11b cells increased after laser-induction of CNV (6.32% vs 1.8%) (data not shown). Because ADM signaling is known to be mediated through CRLR/RAMP2 and CRLR/RAMP3 receptors, we analyzed the expression of CRLR, RAMP2 and RAMP3 mRNA in choroid/RPE complexes after induction of CNV. CRLR, RAMP2 and RAMP3 were highly expressed in the $CD31^+CD45^-$ ECs compared to $CD31^-CD45^-$ non-ECs. However, the level of expression of these ADM receptor components in ECs was not altered after CNV induction compared to sham-operated control groups (Fig. 1G). Moreover, we confirmed the expression of CRLR in the ECs of CNV by immunostaining (Fig. 1H).

Next, we assessed the expression of ADM during CNV formation. In the laser-induced CNV model, the presence of different angiogenic factors in RPE-Choroid complexes has already been reported [22]. We analyzed the expression of ADM mRNA and found that it increased in a time-dependent fashion and peaked 4 days after laser treatment (Fig. 2A). Because it is reported that ADM promotes angiogenesis in both an autocrine and a paracrine manner [8,23], we focused on two cell populations which could be isolated by flow cytometry: $CD31^+$ ECs and $CD11b^+$ monocytes/macrophages. We confirmed that both ECs and macrophages express more ADM mRNA compared to $CD31^-CD11b^-$ cells (Fig. 2B). Furthermore, after CNV induction, ADM expression was significantly upregulated in both ECs and macrophages compared to the same cells in sham-operated mice (Fig. 2C, D). Therefore, these data suggest that ADM is involved in this laser-induced CNV model.

It is well known that inflammatory cytokines upregulate ADM expression in various cells [24,25,26]. We confirmed this by using macrophage (RAW264.7), EC (bEnd.3), and retinal pigment epithelial (ARPE-19) cell lines stimulated with TNF-α and LPS (Fig. 3A). It has been reported that ADM induces EC proliferation, migration and tube formation through phosphatidylinositol 3′ kinase (PI 3′ -kinase)/Akt, extracellular signal-regulated kinase (ERK), and tyrosine phosphorylation of focal adhesion kinase (p125 FAK) [14]. Thus, we tested whether culture supernatant from RAW264.7 cells after TNF-α stimulation promotes EC proliferation and whether this can be inhibited by a widely-accepted ADM antagonist, ADM (22–52) [27]. Although the inhibitory effect was weak compared to a potent VEGF-A signaling inhibitor, SU1498 [28], ADM (22–52) did significantly suppress proliferation of EC cultured not only in supernatant from TNF-α-stimulated macrophages but also to some extent in medium containing TNF-α without macrophages (Fig. 3B). Additionally, we confirmed the absence of the potential toxicity of ADM (22–52) using an in vitro dose-response model (Fig. S1). These data suggest that ADM signaling affects EC proliferation in an autocrine and a paracrine manner. Moreover, we evaluated the expression of ADM in 24 hour-cultured primary RPE/choroid complexes obtained from wild-type mice. TNF-α stimulation of cultured primary RPE/choroid complexes significantly upregulated ADM mRNA and protein levels at the 12 hour time point (Fig. 3C and 3D); however, expression of ADM mRNA after 24 hours was downregulated relative to the 12 hour time point (Fig. 3C). The morphology of the cells did not change(Fig. 3E and 3F).

To clarify the role of ADM in this CNV model, we inhibit ADM signaling using intraocular injections of ADM antagonist, ADM (22–52). Quantification of CNV size judged by immunohistochemical analysis with anti-PECAM-1 Ab 7 days after laser treatment revealed that intraocular injection of ADM (22–52) significantly inhibited the formation of CNV to approximately 60% of controls. In contrast, injection of recombinant ADM did not affect the size of CNV compared to controls, contrary to our expectations (Fig. 4A and B). This suggests that an excessive amount of ADM is produced in the choroid/RPE in this CNV model. Next, we assessed whether the ADM antagonist had any synergistic effect with SU1498 on CNV. Treatment with ADM antagonist and SU1498 together suppressed CNV formation more than SU1498 alone (Fig. 4C). Furthermore, we confirmed the effect of anti-ADM monoclonal antibody; intraocular injection of ADM mAb resulted in significant suppression of CNV formation (Fig. 4D).

Discussion

In the current study, we have explored the possibility that ADM exerts angiogenic effects in a laser-induced CNV model. The ADM receptor was expressed in choroidal endothelial cells and ADM was upregulated in the choroid/RPE complex during CNV formation. Moreover, an ADM pharmaceutical antagonist and a mAb to ADM efficiently suppressed CNV formation and mediated synergistic effects together with a potent VEGF-A inhibitor. These findings suggest that ADM could represent a therapeutic target and be an attractive option for the treatment of CNV in AMD.

The biological functions of ADM are well- recognized to be dilatation of resistance vessels [29,30], increases of cardiac output [31], regulation of vascular permeability [32] and contribution to mobilization, adhesion and differentiation into endothelial progenitor cells of bone marrow-derived cells [33,34,35]. Additionally, several lines of evidence have suggested that inhibiting the ADM pathway with antibodies or antagonists directed against ADM or ADM receptors can reduce angiogenesis and tumor cell proliferation in mouse cancer models [8]. Although ADM is reported to affect not only angiogenesis but also tumor cell proliferation via its autocrine and paracrine mechanisms in cancer, there is little data showing the involvement of ADM in a disease model whose central pathogenesis depends on sprouting angiogenesis [11,12,13,16,23].

ADM immunoreactivity was reported in cardiac myocytes, vascular smooth muscle cells, ECs, renal distal and collecting tubules, mucosal and glandular epithelia of the digestive, respiratory and reproductive system, the endocrine and neuroendocrine system, as well as in the central nervous system [29]. In the current model, upregulation of ADM was not detected in the retina after laser treatment (data not shown), although Blom et al. reported the expression of ADM in neural retina. However, we saw ADM in the RPE/choroid. Secreted inflammatory cytokines after laser burn might be enhancing ADM expression and further accumulation of inflammatory cells.

This was confirmed using a primary RPE/choroid culture model in the present study. However, ADM expression 24 hr after TNF-α stimulation was lower than at 12 hr, in contrast to findings

with different cell lines such as RAW 264.7, RPE-19 and bEnd.3. We hypothesize that this difference can be attributed to the use of transformed cell lines which could display different expression patterns compared to that of primary cultures. Local upregulation of ADM at each photocoagulated site could induce direct ADM effects, i.e. EC proliferation, migration and tube formation. Currently, anti-VEGF therapy has become the major treatment modality for neovascular AMD. However, numerous injections of the anti-VEGF drug may be required to maintain clinical benefit. Moreover, after treatment with anti-VEGF drugs, it can be hypothesized that a hypoxic response could occur and subsequently upregulate ADM, because this has been observed in ECs [25] [36]. Chen et al. reported reciprocal regulation of ADM and HIF-1α expression exerted synergistic effects on proliferation of ECs in vitro [36]. Induction and nuclear translocation of HIF-1 α controls the expression of several angiogenic factors [37]. Therefore, the requirement for additional drugs together with anti-VEGF therapy is rational even if anti-ADM treatment partially suppresses CNV formation.

Although we expected that ADM injection would enhance the angiogenic response, exogenous ADM did not alter the size of CNV. We hypothesize that ADM was already saturated in the lesion and therefore additional factor would not be able to further activate the ADM receptor and exert any greater effects.

Chen et al. reported that tumor-associated macrophages (TAM) express both ADM and ADM receptor components. They also reported that ADM from TAM stimulated ECs and furthered angiogenesis via a paracrine pathway; moreover, it also potentiated the differentiation of TAM from the M1 to M2 state in an autocrine manner [23]. In the current study, infiltrating macrophages in CNV eyes expressed more ADM; therefore we cannot completely exclude the possibility that upregulation of ADM in macrophages could cause them to change their characteristics and to secrete other angiogenic factors such as VEGF. However, the finding of an inhibitory effect on EC proliferation of ADM antagonists in supernatant from macrophage cultures implies that ADM originating from macrophages must be at least partly responsible for CNV formation.

Udono et al. reported that hypoxia and inflammatory cytokines induced the expression of ADM in human RPE cells and that ADM could enhance RPE proliferation [26,38]. Therefore, in this CNV model, it is also possible that ADM expression in RPE was upregulated and that ADM secreted by RPE could promote angiogenesis. However, Huang et al. reported that ADM inhibited the migration of RPE cells in association with reductions in $[Ca^{2+}]$ [39]. Although there is some controversy about the function of ADM in RPE cells, we could demonstrate that inflammatory stimulation up-regulated the expression of ADM in RPE in vitro. Indeed, it is technically difficult to sort the RPE cells by flow cytometry using specific surface markers and we were unable to determine their ADM expression level. Although we have to carefully evaluate the major source of ADM in the CNV model, the observed paracrine and autocrine effects of ADM could induce CNV.

Supporting Information

Figure S1 Toxicity experiment of ADM (22–52) using bEnd.3. proliferation assay. ADM (22–52) could inhibit the proliferation of EC at 10 nM but there was no clear toxicity even at concentration of 100 μM. (*P<0.05).
(TIF)

Acknowledgments

We thank Keisho Fukuhara and Noriko Fujimoto for general assistance.

Author Contributions

Conceived and designed the experiments: SS MK KN NT. Performed the experiments: SS HK HN TW HS. Analyzed the data: SS HK NT DY. Contributed reagents/materials/analysis tools: SS MK KN NT. Wrote the paper: SS NT.

References

1. Dewan A, Liu M, Hartman S, Zhang SS, Liu DT, et al. (2006) HTRA1 promoter polymorphism in wet age-related macular degeneration. Science 314: 989–992.
2. Sakurai E, Anand A, Ambati BK, van Rooijen N, Ambati J (2003) Macrophage depletion inhibits experimental choroidal neovascularization. Invest Ophthalmol Vis Sci 44: 3578–3585.
3. Tsutsumi-Miyahara C, Sonoda KH, Egashira K, Ishibashi M, Qiao H, et al. (2004) The relative contributions of each subset of ocular infiltrated cells in experimental choroidal neovascularisation. Br J Ophthalmol 88: 1217–1222.
4. Xie P, Kamei M, Suzuki M, Matsumura N, Nishida K, et al. (2011) Suppression and regression of choroidal neovascularization in mice by a novel CCR2 antagonist, INCB3344. PLoS One 6: e28933.
5. Xiong M, Elson G, Legarda D, Leibovich SJ (1998) Production of vascular endothelial growth factor by murine macrophages: regulation by hypoxia, lactate, and the inducible nitric oxide synthase pathway. Am J Pathol 153: 587–598.
6. Poyner DR, Sexton PM, Marshall I, Smith DM, Quirion R, et al. (2002) International Union of Pharmacology. XXXII. The mammalian calcitonin gene-related peptides, adrenomedullin, amylin, and calcitonin receptors. Pharmacol Rev 54: 233–246.
7. McLatchie LM, Fraser NJ, Main MJ, Wise A, Brown J, et al. (1998) RAMPs regulate the transport and ligand specificity of the calcitonin-receptor-like receptor. Nature 393: 333–339.
8. Nikitenko LL, Fox SB, Kehoe S, Rees MC, Bicknell R (2006) Adrenomedullin and tumour angiogenesis. Br J Cancer 94: 1–7.
9. Iimuro S, Shindo T, Moriyama N, Amaki T, Niu P, et al. (2004) Angiogenic effects of adrenomedullin in ischemia and tumor growth. Circ Res 95: 415–423.
10. Shindo T, Kurihara Y, Nishimatsu H, Moriyama N, Kakoki M, et al. (2001) Vascular abnormalities and elevated blood pressure in mice lacking adrenomedullin gene. Circulation 104: 1964–1971.
11. Ishikawa T, Chen J, Wang J, Okada F, Sugiyama T, et al. (2003) Adrenomedullin antagonist suppresses in vivo growth of human pancreatic cancer cells in SCID mice by suppressing angiogenesis. Oncogene 22: 1238–1242.
12. Kaafarani I, Fernandez-Sauze S, Berenguer C, Chinot O, Delfino C, et al. (2009) Targeting adrenomedullin receptors with systemic delivery of neutralizing antibodies inhibits tumor angiogenesis and suppresses growth of human tumor xenografts in mice. FASEB J 23: 3424–3435.
13. Ouafik L, Sauze S, Boudouresque F, Chinot O, Delfino C, et al. (2002) Neutralization of adrenomedullin inhibits the growth of human glioblastoma cell lines in vitro and suppresses tumor xenograft growth in vivo. Am J Pathol 160: 1279–1292.
14. Kim W, Moon SO, Sung MJ, Kim SH, Lee S, et al. (2003) Angiogenic role of adrenomedullin through activation of Akt, mitogen-activated protein kinase, and focal adhesion kinase in endothelial cells. FASEB J 17: 1937–1939.
15. Ribatti D, Nico B, Spinazzi R, Vacca A, Nussdorfer GG (2005) The role of adrenomedullin in angiogenesis. Peptides 26: 1670–1675.
16. Hague S, Zhang L, Oehler MK, Manek S, MacKenzie IZ, et al. (2000) Expression of the hypoxically regulated angiogenic factor adrenomedullin correlates with uterine leiomyoma vascular density. Clin Cancer Res 6: 2808–2814.
17. Gavard J, Hou X, Qu Y, Masedunskas A, Martin D, et al. (2009) A role for a CXCR2/phosphatidylinositol 3-kinase gamma signaling axis in acute and chronic vascular permeability. Mol Cell Biol 29: 2469–2480.
18. Campa C, Kasman I, Ye W, Lee WP, Fuh G, et al. (2008) Effects of an anti-VEGF-A monoclonal antibody on laser-induced choroidal neovascularization in mice: optimizing methods to quantify vascular changes. Invest Ophthalmol Vis Sci 49: 1178–1183.
19. Naito H, Kidoya H, Sakimoto S, Wakabayashi T, Takakura N (2011) Identification and characterization of a resident vascular stem/progenitor cell population in preexisting blood vessels. EMBO J 31: 842–855.
20. Takakura N, Watanabe T, Suenobu S, Yamada Y, Noda T, et al. (2000) A role for hematopoietic stem cells in promoting angiogenesis. Cell 102: 199–209.

21. Sakimoto S, Kidoya H, Naito H, Kamei M, Sakaguchi H, et al. (2012) A role for endothelial cells in promoting the maturation of astrocytes through the apelin/APJ system in mice. Development 139: 1327–1335.
22. Grossniklaus HE, Kang SJ, Berglin L (2010) Animal models of choroidal and retinal neovascularization. Prog Retin Eye Res 29: 500–519.
23. Chen P, Huang Y, Bong R, Ding Y, Song N, et al. (2011) Tumor-associated macrophages promote angiogenesis and melanoma growth via adrenomedullin in a paracrine and autocrine manner. Clin Cancer Res 17: 7230–7239.
24. Kubo A, Minamino N, Isumi Y, Katafuchi T, Kangawa K, et al. (1998) Production of adrenomedullin in macrophage cell line and peritoneal macrophage. J Biol Chem 273: 16730–16738.
25. Ogita T, Hashimoto E, Yamasaki M, Nakaoka T, Matsuoka R, et al. (2001) Hypoxic induction of adrenomedullin in cultured human umbilical vein endothelial cells. J Hypertens 19: 603–608.
26. Udono T, Takahashi K, Nakayama M, Murakami O, Durlu YK, et al. (2000) Adrenomedullin in cultured human retinal pigment epithelial cells. Invest Ophthalmol Vis Sci 41: 1962–1970.
27. Saita M, Shimokawa A, Kunitake T, Kato K, Hanamori T, et al. (1998) Central actions of adrenomedullin on cardiovascular parameters and sympathetic outflow in conscious rats. Am J Physiol 274: R979–984.
28. Boguslawski G, McGlynn PW, Harvey KA, Kovala AT (2004) SU1498, an inhibitor of vascular endothelial growth factor receptor 2, causes accumulation of phosphorylated ERK kinases and inhibits their activity in vivo and in vitro. J Biol Chem 279: 5716–5724.
29. Eto T (2001) A review of the biological properties and clinical implications of adrenomedullin and proadrenomedullin N-terminal 20 peptide (PAMP), hypotensive and vasodilating peptides. Peptides 22: 1693–1711.
30. Ishiyama Y, Kitamura K, Ichiki Y, Nakamura S, Kida O, et al. (1993) Hemodynamic effects of a novel hypotensive peptide, human adrenomedullin, in rats. Eur J Pharmacol 241: 271–273.
31. Rademaker MT, Charles CJ, Lewis LK, Yandle TG, Cooper GJ, et al. (1997) Beneficial hemodynamic and renal effects of adrenomedullin in an ovine model of heart failure. Circulation 96: 1983–1990.
32. Hippenstiel S, Witzenrath M, Schmeck B, Hocke A, Krisp M, et al. (2002) Adrenomedullin reduces endothelial hyperpermeability. Circ Res 91: 618–625.
33. Abe M, Sata M, Suzuki E, Takeda R, Takahashi M, et al. (2006) Effects of adrenomedullin on acute ischaemia-induced collateral development and mobilization of bone-marrow-derived cells. Clin Sci (Lond) 111: 381–387.
34. Iwase T, Nagaya N, Fujii T, Itoh T, Ishibashi-Ueda H, et al. (2005) Adrenomedullin enhances angiogenic potency of bone marrow transplantation in a rat model of hindlimb ischemia. Circulation 111: 356–362.
35. Kong XQ, Wang LX, Yang CS, Chen SF, Xue YZ, et al. (2008) Effects of adrenomedullin on the cell numbers and apoptosis of endothelial progenitor cells. Clin Invest Med 31: E117–122.
36. Chen L, Qiu JH, Zhang LL, Luo XD (2012) Adrenomedullin promotes human endothelial cell proliferation via HIF-1alpha. Mol Cell Biochem 365: 263–273.
37. Pugh CW, Ratcliffe PJ (2003) Regulation of angiogenesis by hypoxia: role of the HIF system. Nat Med 9: 677–684.
38. Udono T, Takahashi K, Nakayama M, Yoshinoya A, Totsune K, et al. (2001) Induction of adrenomedullin by hypoxia in cultured retinal pigment epithelial cells. Invest Ophthalmol Vis Sci 42: 1080–1086.
39. Huang W, Wang L, Yuan M, Ma J, Hui Y (2004) Adrenomedullin affects two signal transduction pathways and the migration in retinal pigment epithelial cells. Invest Ophthalmol Vis Sci 45: 1507–1513.

THE JOURNAL OF BIOLOGICAL CHEMISTRY VOL. 288, NO. 18, pp. 12469–12477, May 3, 2013

Ligand-independent Tie2 Dimers Mediate Kinase Activity Stimulated by High Dose Angiopoietin-1*[S]

Received for publication, November 5, 2012, and in revised form, February 19, 2013 Published, JBC Papers in Press, March 15, 2013, DOI 10.1074/jbc.M112.433979

Daishi Yamakawa[‡], Hiroyasu Kidoya[‡], Susumu Sakimoto[‡], Weizhen Jia[‡], Hisamichi Naito[‡], and Nobuyuki Takakura[‡§1]

From the [‡]Department of Signal Transduction, Research Institute for Microbial Diseases, Osaka University, 3-1 Yamada-oka, Suita-shi, Osaka 565-0871, Japan and [§]Japan Science and Technology Agency (JST), Sanbancho, Chiyoda-ku, Tokyo 102-0075, Japan

Background: Tie2 is essential for angiogenesis and vascular stabilization.
Results: Tie2, but not Tie1, forms ligand-independent dimers on the cell surface.
Conclusion: The inactive monomer mutant Tie2YIA/LAS decreases Ang1/Tie2 signaling.
Significance: The Tie2 ligand-independent dimer induces strong phosphorylation upon high dose Ang1 binding.

Tie2 is a receptor tyrosine kinase expressed on vascular endothelial cells (ECs). It has dual roles in promoting angiogenesis and stabilizing blood vessels, and it has been suggested that Tie2 forms dimers and/or oligomers in the absence of angiopoietin-1 (Ang1); however, the mechanism of ligand-independent dimerization of Tie2 and its biological significance have not been clarified. Using a bimolecular fluorescence complementation assay and a kinase-inactive Tie2 mutant, we show here that ligand-independent Tie2 dimerization is induced without Tie2 phosphorylation. Moreover, based on the fact that Tie1 never forms heterodimers with Tie2 in the absence of Ang1 despite having high amino acid sequence homology with Tie2, we searched for ligand-independent dimerization domains of Tie2 by reference to the difference with Tie1. We found that the YIA sequence of the intracellular domain of Tie2 corresponding to the LAS sequence in Tie1 is essential for this dimerization. When the YIA sequence was replaced by LAS in Tie2 (Tie2YIA/LAS), ligand-independent dimer was not formed in the absence of Ang1. When activation of Tie2YIA/LAS was induced by a high dose of Ang1, phosphorylation of Tie2 was limited compared with wild-type Tie2, resulting in retardation of activation of Erk downstream of Tie2. Therefore, these data suggest that ligand-independent dimerization of Tie2 is essential for a strong response upon stimulation with high dose Ang1.

The functions of angiopoietin-1 (Ang1),[2] a ligand for receptor tyrosine kinase Tie2 expressed on endothelial cells (ECs), in both EC-to-EC and EC-to-mural cell adhesion are well established (1–4). Although Ang1-Tie2 signaling is involved in promoting maturation and quiescence of blood vessels mainly regulated by Akt signal transduction via the p85 subunit of PI3K, Tie2 also has proangiogenic activity mediated by MAPK signaling (5–7). Because Tie2 possesses both anti-angiogenic as well as proangiogenic properties, it is important to investigate how Tie2 activation is altered during angiogenesis. The Tie receptor family consists of Tie2 and Tie1 (8–10). Recent studies show that Ang1 activates Tie1 indirectly by interactions with Tie2 (11). When Tie1 expression is silenced, Tie2 signaling especially via the MAPK pathway is enhanced; accordingly, Tie1-deficient mice show hyperproliferative vascular formation and vascular abnormalities (12, 13). This suggests that Tie1 may negatively regulate angiogenic signaling by Tie2.

Tie2 is composed of an extracellular domain, one transmembrane domain, and an intracellular tyrosine kinase domain split into two by a non-kinase sequence. Tie1 has high amino acid sequence homology with Tie2 (76 and 33% identity in intracellular and extracellular domains, respectively). Based on the isolation of Tie2 ligands and analysis of signal transduction through Tie2, it is widely accepted that Ang1 activates Tie2, but Ang2 binding inhibits its signaling. Thus, with certain exceptions Ang2 acts as an Ang1 antagonist (4, 13–18).

It is known that Tie2 is present on the EC surface in the form of dimers and higher order oligomers, as established by electron microscopy (19). It has been reported that EGF receptor, erythropoietin receptor, and TNF receptor also dimerize in a ligand-independent manner (20–25). Ligand-independent dimerization of EGF receptor does not lead to tyrosine phosphorylation of EGF receptor. It has been suggested that a conformational change of the EGF receptor induces kinase activity on ligand binding. Therefore, ligand-independent dimers may mediate rapid signal transduction responses. Although Tie2 also forms ligand-independent dimers, the importance of this has not yet been determined.

In the present study, we established a system for visualization of Tie2 dimers using bimolecular fluorescence complementation (BiFC) assays in living cells (26). Using this system, we sought Ang1-independent Tie2-Tie2 dimerization domains. We generated a Tie2 mutant that does not form dimers in the absence of Ang1. We investigated the biological significance of ligand-independent Tie2 dimerization using this mutant.

* This work was supported in part by a grant from the Ministry of Education, Science, Sports, and Culture of Japan.
[S] This article contains supplemental Table S1 and Figs. S1–S6.
[1]To whom correspondence should be addressed: Dept. of Signal Transduction, Research Institute for Microbial Diseases, Osaka University, 3-1 Yamada-oka, Suita-shi, Osaka 565-0871, Japan. Tel.: 81-6879-8316; Fax: 81-6879-8314; E-mail: ntakaku@biken.osaka-u.ac.jp.
[2]The abbreviations used are: Ang1, angiopoietin-1; EC, endothelial cell; BiFC, bimolecular fluorescence complementation; Ab, antibody.

EXPERIMENTAL PROCEDURES

Reagents and Antibodies—Recombinant human Angl was purchased from R&D Systems. In Western blot analysis, mouse anti-phosphotyrosine (4G10) and anti-Tie2 (Ab33) antibodies (Abs) (Upstate), anti-HA.11 mAb (COVANCE), anti-c-Myc (9E10) and Tiel (C-18) mAbs (Santa Cruz Biotechnology, Inc.), anti-HA-tag rabbit serum (Medical & Biological Laboratories Co., Ltd.), p44/42, phospho-p44/42 (Thr^{202}/Tyr^{204}), phospho-Tie2 (Tyr^{992}) Abs (Cell Signaling Technology, Inc.) and mouse anti-HA (12CA5) mAb (Roche Diagnostics) were used as the first Abs. Anti-phospho-Tie2 (Tyr^{992}) and anti-phosphotyrosine Abs were diluted 1:500, and others were diluted 1:1000. HRP-conjugated anti-rabbit and anti-mouse IgG (Jackson ImmunoResearch Laboratories) was used as the secondary antibody (dilution: 1:1000). For the immunofluorescence analysis, HA and Myc were used as the first Abs (dilution, 1:100). Alexa Fluor 546-conjugated goat anti-rabbit Igs and Alexa Fluor 647-conjugated goat anti-mouse Igs were used as the secondary Abs (Invitrogen) (dilution, 1:200).

Plasmid Construction—Mouse Tie2 and Tiel were fused to sequences encoding full-length Venus and Venus residues 1–173 amino acids (VN) or 155–238 amino acids (VC). The coding regions were connected with linker sequences encoding RSAIT (Arg-Ser-Ala-Ile-Thr). RSAIT is a non-adhesion sequence (26). HA or Myc epitopes were inserted as tags between linker and fluorescent genes. Genes were inserted at the multicloning site in pEGFPN1 vector or pMRX virus vector. Basing the work on the pE-Tie2-linker-Myc-Venus, pE-Tie2-linker-HA-VN and pE-Tie2-linker-Myc-VC, we cut between the BamHI and MluI sites and the Tie2 mutant (Tie2K854R, Tie2R848W) was created. Tie2 kinase-dead (Tie2K854R) or Tie2 constitutive-active (Tie2R848W) mutants were amplified from wild-type Tie2 using Tie2K854R-N, -C primers or Tie2R848W-N, -C primers, respectively (supplemental Table S1).

For the generation of Tiel*, the signal sequence of Tie2 was amplified from the Tie2 plasmid using oligonucleotide primers (forward primer, 5′-GTA GGC GTG TAC GGT GGG AGG TCT-3′ and reverse primer, 5′-GTT AAG TCA ACA GAG CCT TCT ACT ACT CC-3′) and 5′-Tiel core sequence excluding signal sequence was amplified from Tiel using oligonucleotide primers (forward primer, 5′-GGA GTA GTA GAA GGC TCT GTT GAC TTA AC-3′ and reverse primer, 5′-CCA CTT CTG AGC TTC ACA GCC TCG CAC GAT-3′). These two products were amplified with the forward primer for Tie2 and the reverse primer for Tiel. This PCR product was placed into EcoRI and AgeI sites of the Tiel plasmid. For the generation of Tie2/Tiel chimeric plasmids, mutagenesis was performed on Tie2 and Tiel plasmids as templates by using specific primer sets (supplemental Table S1). For generation of 1–3 amino acid mutants of each Tie2 plasmid, mutagenesis was performed using specific primers (supplemental Table S1).

Retroviral Infection—Plat-E cells were transfected with pMRX-Tie2-linker-Myc-Venus, pMRX-Tie2YIA/LAS-linker-Myc-Venus, pMRX-Tie2-linker-HA-VN173 and pMRX-Tie2-linker-Myc-VC155, pMRX-Tie2YIA/LAS-linker-HA-VN173 and pMRX-Tie2YIA/LAS-linker-Myc-VC155 vectors as indicated in each experiment (1.0 μg each) using Lipofectamine 2000 (Invitrogen) and then incubated for 24 h at 37 °C after which the medium was changed. After 12 (36 h from transfection) and 24 h (48 h from transfection), conditioned medium was harvested, sterilized by filtration, and used to infect NIH3T3 cells. 8 μg/ml polybrene was added for enhancement of infection. Stable cell lines were selected by culture in medium containing puromycin (5 μg/ml) or blasticidin (10 μg/ml) (27, 28).

Cell Culture—HEK293T and NIH3T3 lines were grown in DMEM supplemented with 10% FBS. Platinum-E cells (Plat-E; packaging cells) and stable cell lines transfected by pMRX virus vector were cultured in 10% FBS containing DMEM.

Transfection and Bimolecular Fluorescence Complementation Analysis—To carry out BiFC in living cells, cells were co-transfected with the expression vectors indicated in each experiment (1.0 μg each) using Lipofectamine 2000. The fluorescence emissions were acquired in living cells 22–48 h after transfection using a fluorescence microscope with a cooled CCD camera, or by flow cytometry. Protein expression levels were assessed by Western blotting.

Cell Lysis, Immunoprecipitation, SDS-PAGE, and Western Blotting—Cells were washed with ice-cold PBS and lysed with radioimmune precipitation assay lysis buffer (50 mM Tris-HCl, pH 7.5, 150 mM NaCl, 1% Nonidet P-40, 0.5% sodium deoxycholate, 0.1% SDS). The cells were incubated on ice for 10 min followed by centrifugation at 15,000 rpm for 5 min at 4 °C. Cells were immunoprecipitated from the supernatant using 1–2 μg of anti-Myc Ab that had been precoupled to 20 μl of protein A-Sepharose 4 Fast Flow (GE Healthcare).

Proteins electrophoretically separated using 7.5% SDS gels were transferred to nylon membranes (Amersham Biosciences) by a wet blotting procedure (140 V, 200 mA, 120 min). The membrane was blocked with 5% skim milk/TBST for 60 min, subsequently incubated with the Abs as indicated in the figures and processed for chemiluminescence detection with ECL solution. Densitometry was performed with NIH ImageJ software (version 1.43u).

FACS Analysis—BiFC was analyzed by flow cytometry. After fluorescence complementation, cells were washed with PBS and resuspended in PBS. FACS analysis was performed with a FACSCalibur (BD Biosciences) using the 488 nm laser for excitation and a 515–545 nm band pass filter for detection. For quantitative evaluation of BiFC fluorescence, we used % Gated (fluorescent cells) × *X* Geo Mean (average of fluorescent intensity) as arbitrary fluorescence units.

Confocal Laser Scanning Microscopy—Transfected cells on 0.1% gelatin-coated glass dishes (Sigma Aldrich) were rinsed, fixed for 10 min in 4% paraformaldehyde-PBS (pH 7.5), and washed with PBS. Subsequently, the cells were permeabilized with 0.1% Triton X-100 for 10 min. After washing with PBS, cells were blocked with PBS containing 5% normal goat serum and 1% BSA for 30 min and immunostained with first Ab (1:100) for 1 h. Protein reacting with Ab was visualized with secondary Abs (1:200). HA or Myc epitopes were inserted as tags between Tie2 or Tie2YIA/LAS and the BiFC tag (VN or VC). HA-VN fused with Tie2 or Tie2YIA/LAS was stained by rabbit anti-HA Ab (Medical & Biological Laboratories Co., Ltd.) and Alexa Fluor 546 (red)-conjugated anti-rabbit Igs. Myc-VC fused with Tie2 or Tie2YIA/LAS was stained with

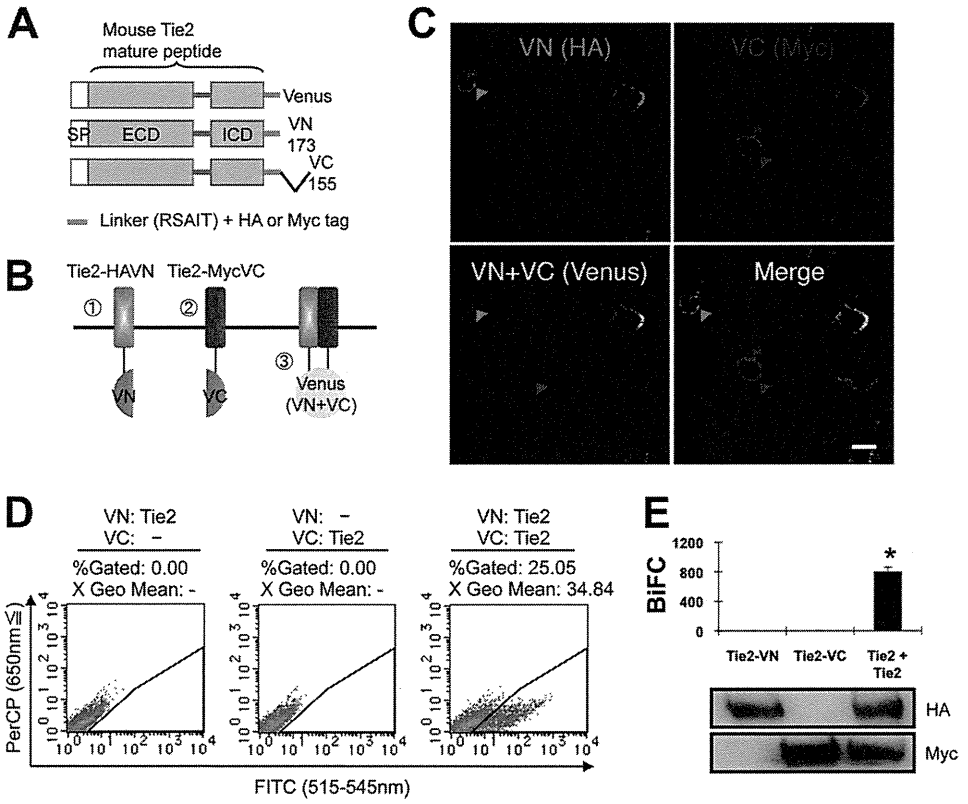

FIGURE 1. **BiFC analysis of Tie2 receptor homodimerization in living cells.** *A* and *B*, schematic representation of Tie2 tagged with either the N- or C-terminal of the Venus fragment (VN or VC). *SP*, signal peptide; *ECD*, extracellular domain; *ICD*, intracellular domain. When Tie2 dimerizes, fluorescence should reconstitute. *C*, HEK293T cells expressing Tie2-HAVN (*red*) and Tie2-MycVC (*blue*) observed by confocal microscopy. Cells were co-transefected with Tie2-HAVN and Tie2-MycVC expression vectors. Note that cells expressing Tie2-HAVN alone (*red arrowhead*) or Tie2-MycVC alone (*blue arrowhead*) develop no Venus fluorescence. *Bar* indicates 20 μm. *D*, flow cytometric analysis for evaluation of receptor dimerization as indicated. *E*, quantitative evaluation of Tie2 homodimerization in BiFC as observed in *D* (*, $p < 0.05$; $n = 3$). Protein expression level of each receptor was assessed by immunoblotting with anti-HA or anti-Myc Ab.

mouse anti-Myc Ab and Alexa Fluor 647 (blue)-conjugated anti-mouse Igs. BiFC fluorescence was detected using a filter for Alexa Fluor 488 (green). The slides were observed under a Leica TCS SP5 Ver1.6 (Leica Microsystems) using HCX PL APO lambda blue 63 × 1.4 oil. Images were processed using Adobe Photoshop CS5 Extended software (Adobe Systems).

Statistical Analysis—All data are displayed as the mean ± S.D. and were analyzed by two-tailed Student *t* test. A probability value of < 0.05 was considered statistically significant.

RESULTS

Establishment of Imaging Methods for Investigating the Dimerization of Tie2 Receptors—It has been reported that Tie2 is present in the form of dimers and/or oligomers on the cell surface (19). We also detected ligand-independent dimers of endogenous Tie2 in human umbilical vein endothelial cells (supplemental Fig. S1*A*). To assess Tie2 dimerization in the absence of Angl, we utilized the BiFC assay (26). First, we prepared amino (N)-terminal (1–173: VN173) and carboxyl (C)-terminal (155–238: VC155) components of Venus fluorescent protein, a modifier of yellow fluorescent protein, fused with the C-terminal domain of wild-type (WT) mouse Tie2 with an HA or Myc tag linked to the molecule (Fig. 1*A*). When Tie2 (Tie2-HAVN, Tie2-MycVC) dimerizes, the fluorescent complex should be reconstituted (Fig. 1*B*). As expected, when Tie2-HAVN and Tie2-MycVC were cotransfected into HEK293T cells, cells expressing both HA and Myc developed fluorescence (Fig. 1*C*). Flow cytometry showed that transfection with both Tie2-HAVN and Tie2-MycVC vectors, but not with either alone, resulted in cells having high FITC intensity (Fig. 1, *D* and *E*). We confirmed that these co-transfectants developed BiFC fluorescence in cells expressing physiological levels of Tie2 as observed in ECs (supplemental Fig. S1, *B* and *C*).

Analysis of the Dimerization of Tie2-Tie1 using BiFC Assays—Angl activates Tie1 indirectly, mediated by its interaction with Tie2 (11, 12). It has been suggested that co-localization of Tie2 and Tie1 is induced upon activation of Tie2 by Angl (6). We investigated whether Tie2 and Tie1 also form heterodimers in a ligand-independent manner. Relative to Tie2, we found that the Tie1 protein was difficult to express in HEK293T cells following transfection of full-length Tie1 cDNA. However, when the original native signal sequence of Tie1 was excised and replaced with the Tie2 signal sequence (designated Tie1*), Tie1 expression was easily induced (Fig. 2*A*). Using this Tie1* construct, we evaluated Tie2-Tie1 and Tie1-Tie1 associations by BiFC. Although it has recently been reported that Tie2 and Tie1 associate following Angl stimulation and on cell-cell contact, we failed to detect any Tie2-Tie1 or Tie1-Tie1 associations (Fig. 2, *B–D*). This suggests that a Tie2 and Tie1 interaction is required for Angl binding to Tie2 and Tie1 and that Tie1 never gives rise to inactive dimers and/or oligomers in the absence of Angl.

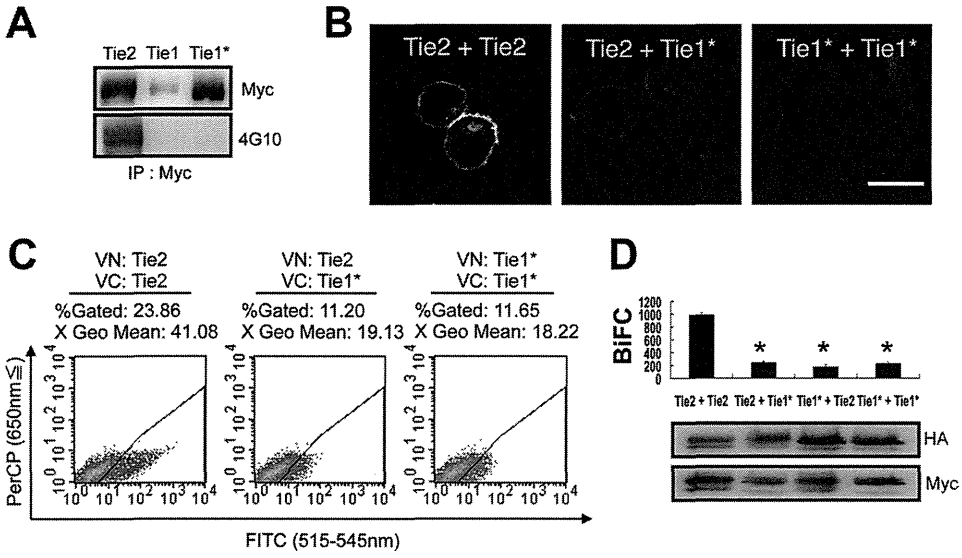

FIGURE 2. **BiFC analysis comparing Tie2 and Tie1*.** *A*, signal peptide of Tie1 was replaced with that of Tie2 (Tie1*). All receptors were C-terminally tagged with Myc. The levels of Tie2, Tie1, and Tie1* protein were analyzed with Myc or 4G10 Ab. *B–D*, HEK293T cells were transiently transfected in combination with Tie2-HAVN and Tie2-MycVC, Tie2-HAVN and Tie1*-MycVC, or Tie1*-HAVN and Tie1*-MycVC. *B*, cells were analyzed by confocal microscopy. *Bar* indicates 20 μm. *C*, flow cytometric analysis for evaluation of receptor dimerization as indicated. *D*, quantitative evaluation of receptor dimerization in BiFC as shown in *C* (*, $p < 0.05$; $n = 3$). Protein expression level of each receptor was assessed by immunoblotting with anti-HA or anti-Myc Ab.

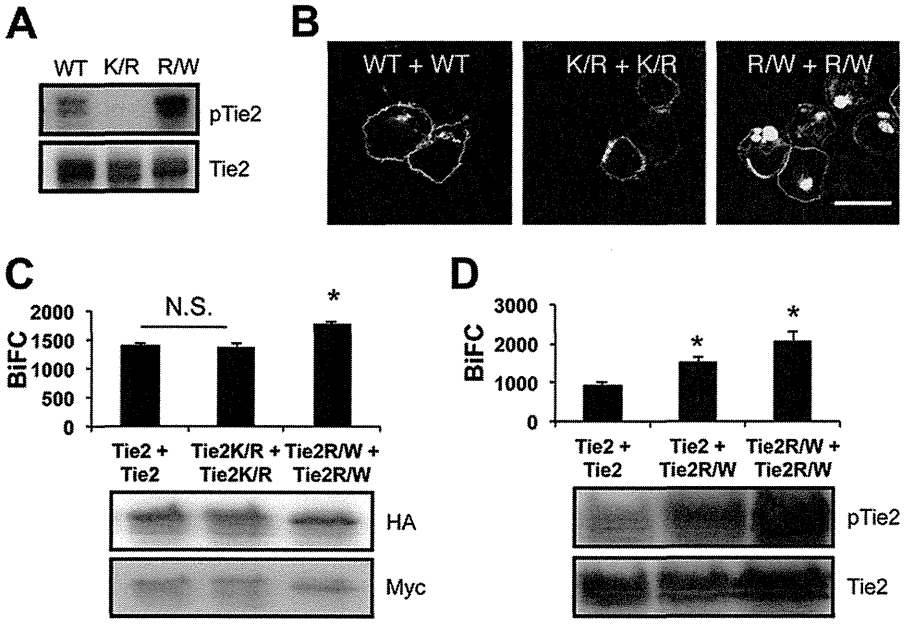

FIGURE 3. **BiFC analysis comparing Tie2 and Tie2 mutant.** *A*, detection of Tie2, kinase-dead mutant Tie2K854R (*K/R*) and constitutively active mutant Tie2R848W (*R/W*) phosphorylation. *B* and *C*, HEK293T cells were transiently transfected in combination with Tie2-HAVN and Tie2-MycVC, Tie2K854R-HAVN and Tie2K854R-MycVC, or Tie2R848W-HAVN and Tie2R848W-MycVC. *B*, cells were analyzed by confocal microscopy. *Bar* indicates 20 μm. *C*, quantitative evaluation of receptor dimerization in BiFC as shown in *B* (*, $p < 0.05$; $n = 3$). Protein expression level of each receptor was assessed by immunoblotting with anti-HA or anti-Myc Ab. *D*, quantitative evaluation of receptor dimerization in BiFC of Tie2 and Tie2R848W (*, $p < 0.05$; $n = 3$). Protein expression level of each receptor was assessed by immunoblotting with anti-Tie2. *N.S.*, not significant.

Analysis of the Dimerization of Tie2 Mutants Using BiFC Assays—Phosphorylation of overexpressed Tie1 and Tie2 was observed, but only Tie2 and not Tie1 was autophosphorylated in the absence of Ang1 stimulation (Fig. 2*A*). To test whether phosphorylation of Tie2 affects Tie2-Tie2 dimerization, we generated a kinase-inactive Tie2 mutant (Tie2K854R) (Fig. 3*A*). However, loss of phosphorylation did not affect Tie2 dimerization (Fig. 3, *B* and *C*, and supplemental Fig. S2A). We further confirmed that it was not until Ang1 bound Tie2 that dimerized Tie2 was internalized (supplemental Fig. S2*B*). Although dimerized WT Tie2 was observed in the cytoplasm, dimerized kinase-inactivated Tie2 did not internalize from the cell surface into the cytoplasm (Fig. 3*B*). Next, we constructed a constitutively active mutant of Tie2 (Tie2R848W) (Fig. 3*A*) (29). In HEK293T cells overexpressing Tie2R848W-HAVN and Tie2R848W-MycVC, more abundant Venus fluorescence was observed in the cytoplasm than in wt Tie2 or Tie2K854R (Fig. 3, *B* and *C*). Interestingly, Tie2R848W can dimerize with WT Tie2, resulting in BiFC intensity enhanced compared with Tie2-Tie2 dimers (Fig. 3*D*). These results suggest that our BiFC

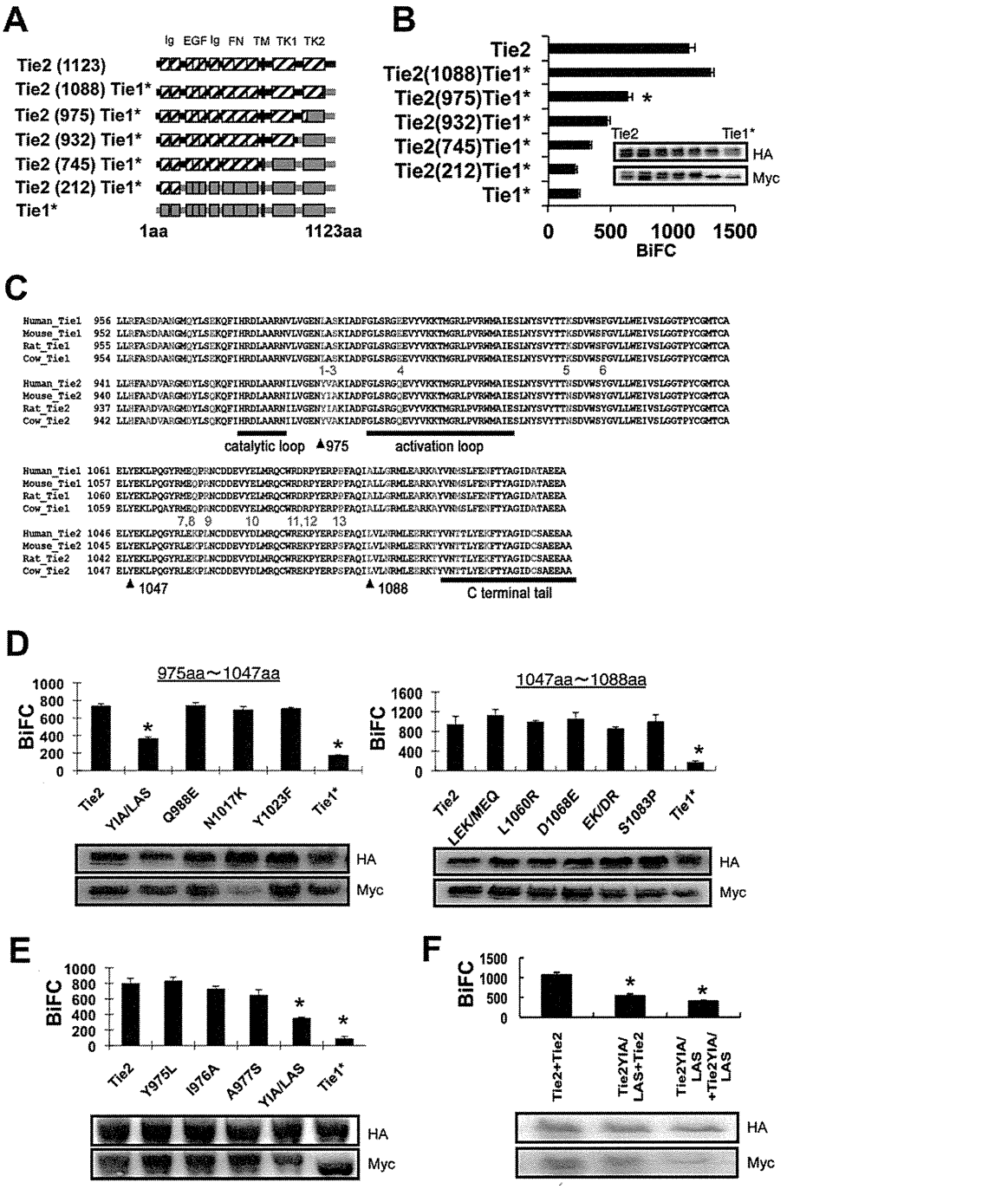

FIGURE 4. **YIA sequence of Tie2 induces ligand-independent dimerization.** *A*, schematic of Tie2/Tie1* chimeras. *B*, in HEK293T cells, Tie2-HAVN was transiently transfected in combination with Tie2, Tie2(1088)Tie1*, Tie2(975)Tie1*, Tie2(932)Tie1*, Tie2(745)Tie1*, Tie2(212)Tie1*, or Tie1* C-terminally fused with MycVC, and close associations of receptors assessed by BiFC and flow cytometry (*, $p < 0.05$; $n = 3$). The protein expression level of each receptor was confirmed by immunoblotting with anti-HA or anti-Myc Ab (*inset*). *C*, comparison of amino acid sequences of Tie1 and Tie2 C terminus from different species. *Pink*, different amino acids; *blue*, same amino acids (*aa*). *D* and *E*, in HEK293T cells, Tie2-HAVN was transiently transfected in combination with Tie2, Tie2YIA/LAS, Tie2Q988E, Tie2N1017K, Tie2Y1023F, Tie2LEK/MEQ, Tie2L1060R, Tie2D1068E, Tie2EK/DR, Tie2S1083P, or Tie1* C-terminally fused with MycVC (*D*) or Tie2, Tie2Y975L, Tie2I976A, Tie2A977S, Tie2YIA/LAS, or Tie1* C-terminally fused with MycVC (*E*), and close associations of receptors assessed by BiFC and flow cytometry. Protein expression level of each receptor was confirmed by immunoblotting with anti-HA or anti-Myc Ab (*inset*) (*, $p < 0.05$; $n = 3$). *F*, YIA domain of Tie2 was replaced by LAS sequence (Tie2YIA/LAS). Association of Tie2-Tie2, Tie2-Tie2YIA/LAS, and Tie2YIA/LAS-Tie2YIA/LAS was observed by BiFC as described above. Protein expression level of each receptor was confirmed by immunoblotting with anti-HA or anti-Myc Ab (*inset*) (*, $p < 0.05$; $n = 3$).

system mimics canonical receptor down-modulation only after activation of the receptor.

Identification of the Domain That Induces Ligand-independent Tie2 Homodimerization—We found that Tie2, but not Tie1, forms homodimers in a ligand-independent manner. Hence, we attempted to isolate the Tie2 ligand-independent dimerizing region. First, we sought domains responsible for Tie2-Tie2 association by replacing part of Tie2 with the Tie1 homologous domain (Fig. 4*A*). We found that lack of the extracellular domain of Tie2 did not affect BiFC (supplemental Fig. S3), suggesting that BiFC caused by Tie2-Tie2 interaction is mainly induced by the intracellular domain of Tie2 in our